Chapter 8
Electrodeposited Alloy Powders

8.1 Introduction

The alloy powders of the iron-group metals (anomalous codeposition) are of great interest for many industrial applications [1]. The Co-Ni powders showed significant promise for future development of hard magnetic materials, commercial batteries, catalysts, catalyzing electroplates, hydrogen-absorbing alloy anodes, and magnetoresistive sensors, being made by several different techniques [1]. Unfortunately, limited number of papers concerning Co-Ni powder electrodeposition exists in the literature [2–7]. As shown in some of these papers [4–7], the morphology and composition of electrodeposited powders were found to be sensitive to the solution composition (to the ratio of Ni^{2+}/Co^{2+} ion concentration). Fe-Ni-based alloy powders are known as promising soft magnetic materials with low coercivity and high permeability [1]. Electrodeposition of Fe-Ni alloy powders was the subject of only few papers [8–12]. The influence of the composition of electrolyte (Ni^{2+}/Fe^{2+} ions ratio) on the powder morphology was investigated in Ref. [8, 9]. Zhelibo et al. [10, 11] suggested a method for producing very fine Fe-Ni alloy powder by the electrolysis in a two-layer electrolytic bath, using a hydrocarbon solvent from an oil-refining fraction as an upper organic layer with evaporation at 180 °C and subsequent reduction annealing in a hydrogen atmosphere. The influence of the reduction annealing temperature [10] and the electrolysis temperature [11] on the formation, chemical and phase composition, structure, and magnetic properties of highly dispersed Fe-Ni alloy powders was investigated, and the optimal thermal conditions for the production of powders with micro-sized particles were determined [10, 11]. The effect of complexing agents (citric and oxalic acid) on the process of Fe-Ni alloy powder electrodeposition was also investigated [12]. It was shown that complexing agents influence the kinetics of powder electrodeposition as well as the morphology of the Fe-Ni powders. Finer powders were produced in the presence of citric acid in comparison with those obtained in the presence of oxalic acid [1, 12].

K.I. Popov et al., *Morphology of Electrochemically and Chemically Deposited Metals*, DOI 10.1007/978-3-319-26073-0_8

The Mo-Ni alloys (induced codeposition) possess several useful properties, with the most important one being exceptional corrosion and wearing resistance [1]. The Mo-Ni alloys can be produced by several methods, from which metallurgical ones are not convenient because of easy oxidation and high melting temperature of molybdenum. The powder metallurgy and mechanical alloying, spark plasma sintering, and laser cladding are mostly used for the Mo-Ni alloy preparation [1].

All abovementioned methods are expensive in comparison with the electrodeposition of Mo-Ni alloy coatings. Although molybdenum cannot be separately electrodeposited from aqueous solutions, it can be codeposited with the iron-group metals (Fe, Co, Ni) in the presence of appropriate complexing agents, by the type of alloy electrodeposition defined by Brenner [13] as induced codeposition.

It should be emphasized here that only two papers concerning electrodeposition of Mo-Ni alloy powders (actually powders of the system Mo-Ni-O) and their characterization are published so far [14–16].

8.2 Anomalous Codeposition of Alloy Powders

8.2.1 Electrodeposited Co-Ni Powders

Electrodeposition of Co-Ni powders was performed in two types of ammonium hydroxide containing electrolytes: 1 M $(NH_4)_2SO_4 + 0.7$ M NH_4OH and 1 M $NH_4Cl + 0.7$ M NH_4OH. In sulfate-containing electrolytes, cobalt and nickel sulfates were used, while in chloride-containing electrolytes, cobalt and nickel chlorides were used as a source of Co^{2+} and Ni^{2+} ions [3–6]. The Co-Ni alloy powders were also electrodeposited from a solution containing 0.4 M $H_3BO_3 + 0.2$ M Na_2SO_4 and Ni and Co sulfate salts [7]. Three different Ni^{2+}/Co^{2+} concentration ratios were used: (1) $Ni^{2+}/Co^{2+} = 1.00$ (0.01 M $NiSO_4$/0.01 M $CoSO_4$); $Ni^{2+}/Co^{2+} = 0.50$ (0.01 M $NiSO_4$/0.02 M $CoSO_4$); $Ni^{2+}/Co^{2+} = 0.33$ (0.01 M $NiSO_4$/0.03 M $CoSO_4$). From these solutions, Co-Ni alloy powders were electrodeposited at a constant current density of approximately 70 mA cm^{-2}, corresponding to the cell voltage of about 5.0 V [7].

8.2.1.1 Polarization Curves for Co-Ni Alloy Powder Electrodeposition from the Sulfate-Containing Supporting Electrolyte

In Fig. 8.1a are shown polarization curves corrected for IR drop for the processes of Co, Ni, and Co-Ni alloy powder electrodeposition from 1 M $(NH_4)_2SO_4 + 0.7$ M NH_4OH containing supporting electrolyte. Their shape of all polarization curves is identical, characterized with two inflection points, A and B. For Co electrodeposition, sharp increase of current occurs at about −1.19 V versus Ag/AgCl, while for Ni electrodeposition, this phenomenon is moved to more negative potentials

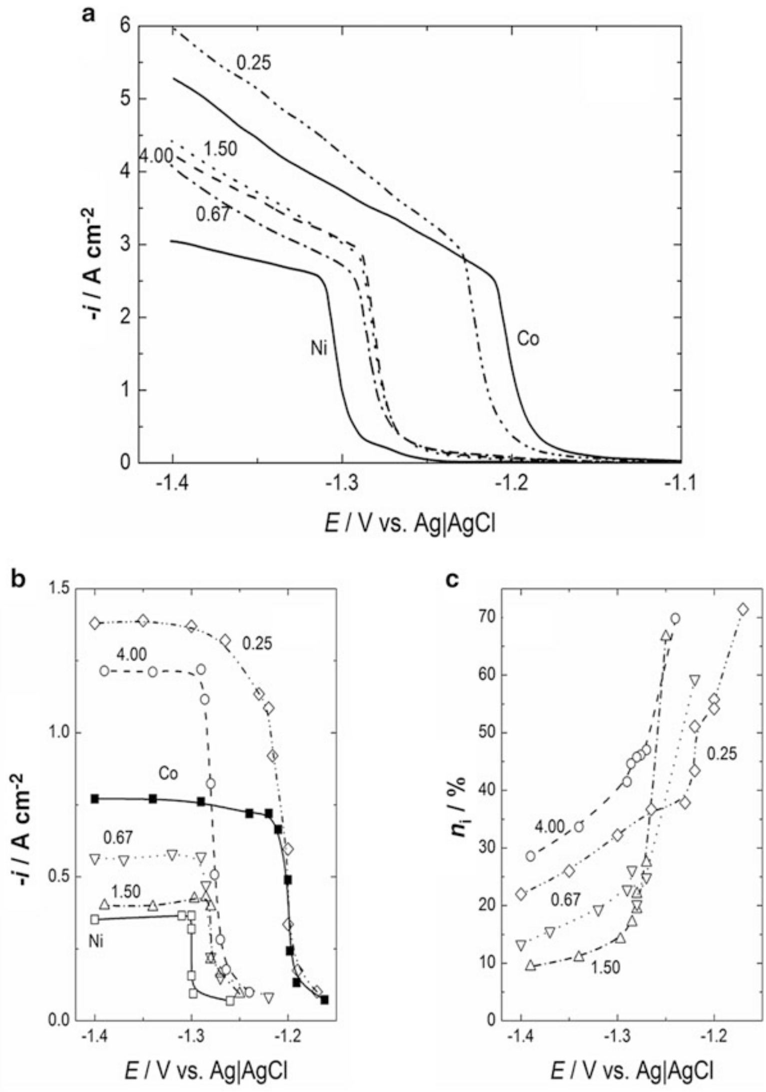

Fig. 8.1 (**a**) Polarization curves for the electrodeposition of cobalt (Co), nickel (Ni), and Co-Ni alloy powders after IR drop correction recorded for different Ni^{2+}/Co^{2+} ions ratios: 4.00, 1.50, 0.67, and 0.25 (marked in the figure). (**b**) The same polarization curves after hydrogen evolution current density subtraction. (**c**) Corresponding η_i vs. E curves for (**b**) (Reprinted from Ref. [1] with kind permission from Springer)

(at about −1.30 V versus Ag/AgCl), indicating that the overpotential for Ni electrodeposition in this solution is for about 0.1 V higher than that for Co electrodeposition, as it is the case for hydrogen evolution from pure supporting electrolytes [1]. In the case of alloy electrodeposition, sharp increase of current density on the polarization curves recorded for Ni^{2+}/Co^{2+} ratios 4.00, 1.50, and 0.67 takes place at almost identical potentials, while the one for $Ni^{2+}/Co^{2+} = 0.25$ is moved to more positive potential, close to the polarization curve for pure Co.

Polarization curves corresponding only to the processes of electrodeposition of pure metals and alloy powders (after subtracting hydrogen evolution current density) are shown in Fig. 8.1b. Corresponding η_i vs. E curves for alloy powder electrodeposition are presented in Fig. 8.1c. It is interesting to note that the current density plateaus (diffusion-limiting current densities) for the electrodeposition of Co-Ni alloys at the Ni^{2+}/Co^{2+} ratios 4.00 and 0.25 are higher than that for pure Co electrodeposition (Fig. 8.1b). The reason for such behavior is the fact that the total concentration of cations in these two solutions was not 0.1 M, since the compositions of these solutions were 0.1 M $NiSO_4 + 0.025$ M $CoSO_4 + 1$ M $(NH_4)_2SO_4 + 0.7$ M NH_4OH and 0.025 M $NiSO_4 + 0.1$ M $CoSO_4 + 1$ M $(NH_4)_2SO_4 + 0.7$ M NH_4OH (total concentration of cations 0.125 M). At the same time, the current efficiency for Co-Ni powder electrodeposition is the highest in these two solutions. Such behavior is most probably the consequence of the independence of the current density for hydrogen evolution on the total concentration of cations, so that the same curve for hydrogen evolution is subtracted from the higher values of total current densities for alloy powder electrodeposition [1].

8.2.1.2 The Morphology of the Co-Ni Alloy Powders Electrodeposited from the Sulfate-Containing Supporting Electrolyte

The morphology of the Co-Ni alloy powders electrodeposited at the current density $i = -0.5$ A cm^{-2} from the electrolytes containing different Ni^{2+}/Co^{2+} ions ratio is shown in Figs. 8.2, 8.3, 8.4, and 8.5. It is obvious that the morphology of Co-Ni alloy powder is sensitive to the Ni^{2+}/Co^{2+} ions ratio, i.e., to the composition of the alloy powder.

In the powder containing the highest amount of Ni, of about 64 at.% Ni, electrodeposited at the $Ni^{2+}/Co^{2+} = 4.00$, more than 90 % of agglomerates were typical spongy agglomerates varying in the size from about 50 μm to about 200 μm, shown in Fig. 8.2. Very few cauliflower-like agglomerates of slightly different shape than those typical for pure Ni powder were also detected in the alloy powder. One such particle is marked with the arrow in the upper right corner of Fig. 8.2. It is important to note that this particle has a flat surface on one side, indicating that this type of growth belongs to the beginning of the powder formation with this particle being detached from the electrode surface before the bigger, typical spongy agglomerate is formed. Spongy agglomerates are more similar to the ones detected in pure Co powder, with the presence of large number of cavities, but contrary to the situation in the case of pure Co powder [1], here practically none of the cavities possess fern-like dendrites on their bottom, indicating that most of the agglomerates has been detached from the electrode surface before the hydrogen bubble in the cavity was liberated. It is interesting that practically no dendrites are found in this powder, although about 26 wt.% of Co are present in the powder.

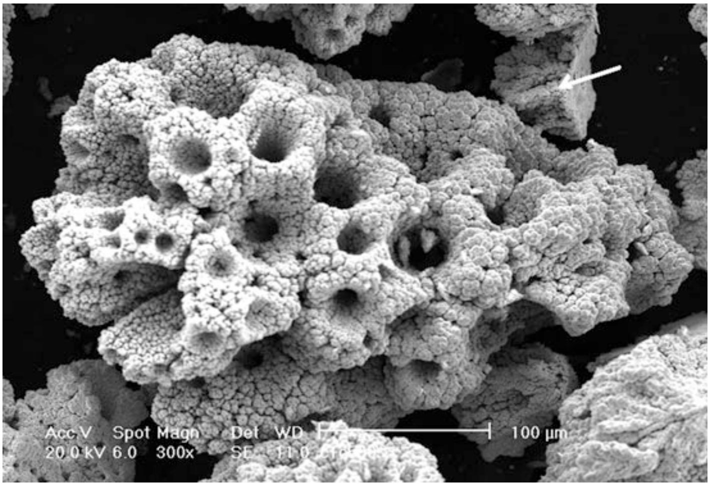

Fig. 8.2 Typical powder particle detected in the powder electrodeposited at the $Ni^{2+}/Co^{2+} = 4.00$ (Reprinted from Ref. [1] with kind permission from Springer)

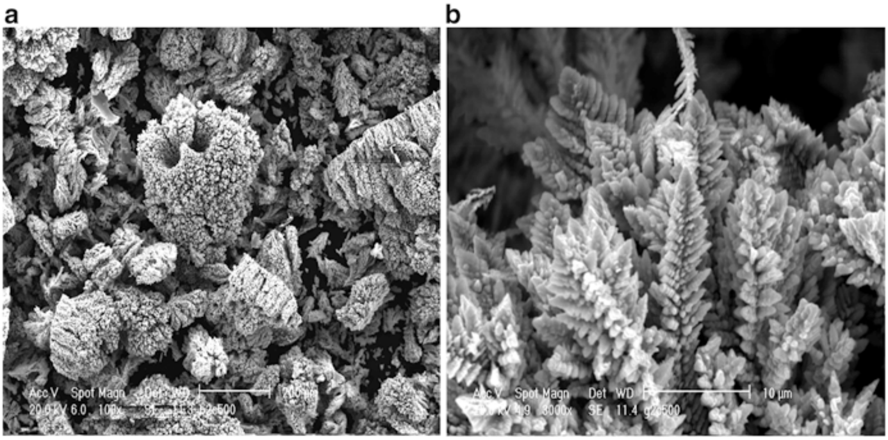

Fig. 8.3 Typical powder agglomerates detected in the powder electrodeposited at the $Ni^{2+}/Co^{2+} = 1.50$. (**a**) Few bigger aglomerates (about 200 µm). Number of cavities significantly reduced in comparison with the one presented in Fig. 8.2. (**b**) Fern-like dendrites covering all agglomerates (Reprinted from Ref. [1] with kind permission from Springer)

As the Ni^{2+}/Co^{2+} ions ratio in the electrolyte decreases from 4.00 to 1.50, the composition of the Co-Ni alloy powder changes from about 78 at.% Ni – 22 at.% Co to about 56 at.% Ni – 44 at.% Co, and this change influences the morphology of the powder. All powder agglomerates electrodeposited at $Ni^{2+}/Co^{2+} = 1.50$ are covered with the fern-like dendrites (Fig. 8.3b). Only few of agglomerates are bigger (about 200 µm), and the number of cavities observed on them is significantly

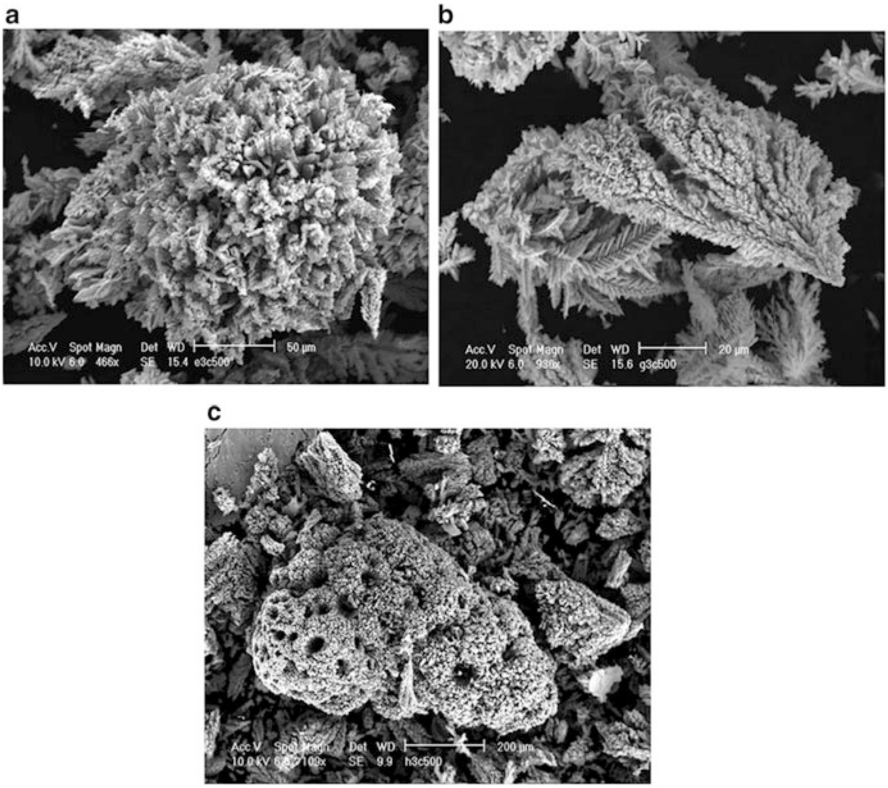

Fig. 8.4 Typical powder agglomerates detected in the powder electrodeposited at the $Ni^{2+}/Co^{2+} = 0.67$. (**a**) Agglomerate covered with fern-like dendrites, (**b**) Higher amount of dendritic particles around the agglomerates, (**c**) Compact agglomerate covered with small fern-like dendrites and the presence of cavities (Reprinted from Ref. [1] with kind permission from Springer)

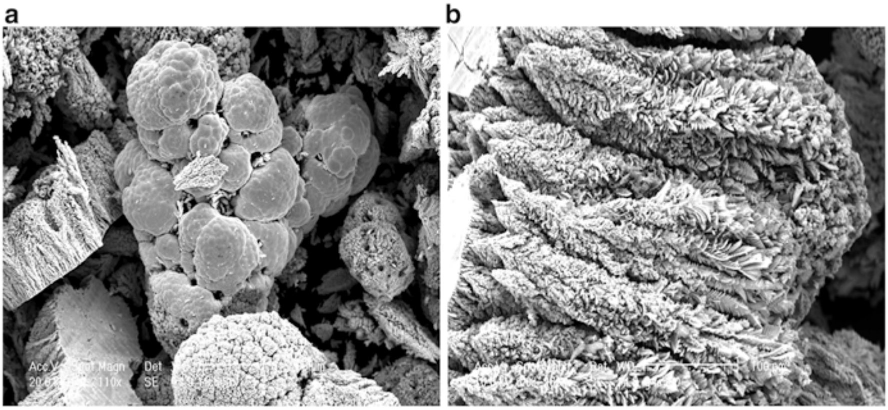

Fig. 8.5 Typical powder agglomerates detected in the powder electrodeposited at the $Ni^{2+}/Co^{2+} = 0.25$. (**a**) Spongy-like agglomerates of the size of about 500 μm covered with the fern-like dendrites, (**b**) Agglomerates composed of closely packed fern-like dendrites about 200 μm long (Reprinted from Ref. [1] with kind permission from Springer)

reduced (Fig. 8.3a) in comparison with the one obtained at the ratio $Ni^{2+}/Co^{2+} = 4.00$. As can be seen in Fig. 8.3a, the significant number of dendritic agglomerates is detected in this powder deposit (around the agglomerate). Very few spongy-like agglomerates of the size of about 500 μm are also present in the powder, and they are also covered with the fern-like dendrites, indicating that the presence of higher amount of Co in the powder, dendritic growth prevails. With further decrease of the Ni^{2+}/Co^{2+} ions ratio (0.67) in the electrolyte, the composition of the Co-Ni alloy powder changes toward lower content of Ni, and the morphology of powder agglomerates is slightly different. In this case, the number of agglomerates increases in comparison with the ratio $Ni^{2+}/Co^{2+} = 1.50$, with the shape of agglomerates being different, as can be seen in Fig. 8.4a–c. A common characteristic of all agglomerates obtained at $Ni^{2+}/Co^{2+} = 0.67$ is that they are covered with the fern-like dendrites. At the same time, higher amount of dendritic particles (around the agglomerate shown in Fig. 8.4b) is formed during Co-Ni powder electrodeposition. The size of dendrite particles varies from about 5 μm to about 50 μm.

In the Co-Ni alloy powder electrodeposition with the highest percentage of Co (85 at.%), Fig. 8.5, different types of agglomerates could be detected: (*i*) spongy-like agglomerates of the size of about 500 μm covered with the fern-like dendrites, also found in the powder obtained at $Ni^{2+}/Co^{2+} = 0.67$ (Fig. 8.4c); (*ii*) compact agglomerates, characteristic for pure Co powder (Fig. 8.5a); and (*iii*) agglomerates composed of closely packed fern-like dendrites about 200 μm long (Fig. 8.5b). By the EDS analysis of the compact agglomerate, shown in Fig. 8.5a, it is found that it does not represent pure Co particle, but the Co-Ni alloy of almost identical composition as the rest of the powder, indicating that the formation of alloy agglomerates follows a growth mechanism for Co powder formation [1, 3].

Considering all detected types of agglomerates in electrodeposited Co-Ni alloy powders of different compositions, one can conclude that only one powder (with 78 at.% of Ni) contains very small amount of cauliflower-like agglomerates typical for pure Ni powder, but slightly different, while the rest of them contain some of the agglomerates detected in pure Co powder. The difference between the agglomerates detected in pure Co powder and in Co-Ni alloy powder (except for the agglomerates obtained from the electrolyte with the highest Ni^{2+}/Co^{2+} ions ratio, Fig. 8.1) is the presence of fern-like dendrites on the surface of these agglomerates. Such a behavior indicates that for these three alloy compositions the presence of Ni^{2+} and Co^{2+} ions promotes dendrite formation on the surface of all agglomerates detected in Co-Ni alloy powders. Hence, it appears that although some similarities between the type of agglomerates detected in pure Co and Co-Ni alloy powders exist, it is practically not possible to strictly correlate composition of alloy powders with their morphology [1].

In order to explain the difference in the morphology as a function of alloy composition (Ni^{2+}/Co^{2+} ions ratio), one should refer to the polarization curves presented in Fig. 8.1b. As can be seen in this figure, at the applied current density of -0.5 A cm^{-2}, only one alloy, obtained from the solution containing $Ni^{2+}/Co^{2+} = 1.50$, electrodeposits at its diffusion limiting current density. The one obtained at the $Ni^{2+}/Co^{2+} = 0.67$ electrodeposits at a slightly lower current density than its diffusion limiting current density, while for the alloys electrodeposited at $Ni^{2+}/Co^{2+} = 4.00$ and 0.25, applied current density lies in the region of mixed control of electrodeposition, being much less than the diffusion limiting current density for those electrolyte compositions. Bearing in mind that the currents presented in this figure represent only 20 % of the total current and that massive hydrogen evolution takes place together with the process of alloy electrodeposition, it is quite difficult to find good explanation for the phenomena observed. Different theories concerning powder formation during metal electrodeposition exist in the literature [1] with one of them claiming that powder formation takes place at the diffusion limiting current at potentials of hydrogen evolution, which is necessary process for powder formation. In the case of Co-Ni alloy powder electrodeposition, hydrogen evolution commences already at the beginning of the electrodeposition process, being catalyzed by the electrodeposition. Hence, any comparison between these two processes is not realistic, but it is obvious that hydrogen evolution plays an important role in the process of powder electrodeposition.

8.2.1.3 Polarization Curves for Co-Ni Alloy Powder Electrodeposition from the Chloride-Containing Supporting Electrolyte

The polarization curves corrected for IR drop for the processes of pure cobalt (Co), pure nickel (Ni), and Co-Ni alloy (powders) electrodeposition from ammonium chloride–ammonium hydroxide (1 M $NH_4Cl + 0.7$ M NH_4OH) containing supporting electrolyte are presented in Fig. 8.6a (in this case, total concentration of cations in all investigated solutions was 0.1 M). As can be seen, cobalt electrodeposition (Co) commences at about −1.1 V versus Ag/AgCl, while sharp increase of current density (massive Co electrodeposition and hydrogen evolution) occurs at about −1.19 V versus Ag/AgCl. In the case of nickel electrodeposition (Ni), sharp increase of current density is moved to more negative potentials (at about −1.30 V versus Ag/AgCl), indicating that the overvoltage for massive Ni electrodeposition (and hydrogen evolution) in this solution is for about 0.1 V higher than that for Co electrodeposition, as it is the case for hydrogen evolution from pure supporting electrolytes [1]. In the case of Co-Ni alloy powder electrodeposition, polarization curves recorded for all Ni^{2+}/Co^{2+} ratios are placed between the polarization curves for pure Co and pure Ni.

Polarization curves corresponding only to the processes of electrodeposition of pure metals and alloy powders (after subtracting hydrogen evolution current density) are shown in Fig. 8.6b. Corresponding η_i vs. E curves for pure metals and alloy powder electrodeposition are presented in Fig. 8.6c [1].

As in the case of sulfate-supporting electrolyte (Fig. 8.1b), “diffusion limiting current density” (in this case not represented with the plateau) for Co is higher than that for Ni (Fig. 8.6b). At the same time, all polarization curves for Co-Ni alloy powder electrodeposition are characterized with higher values of current densities,

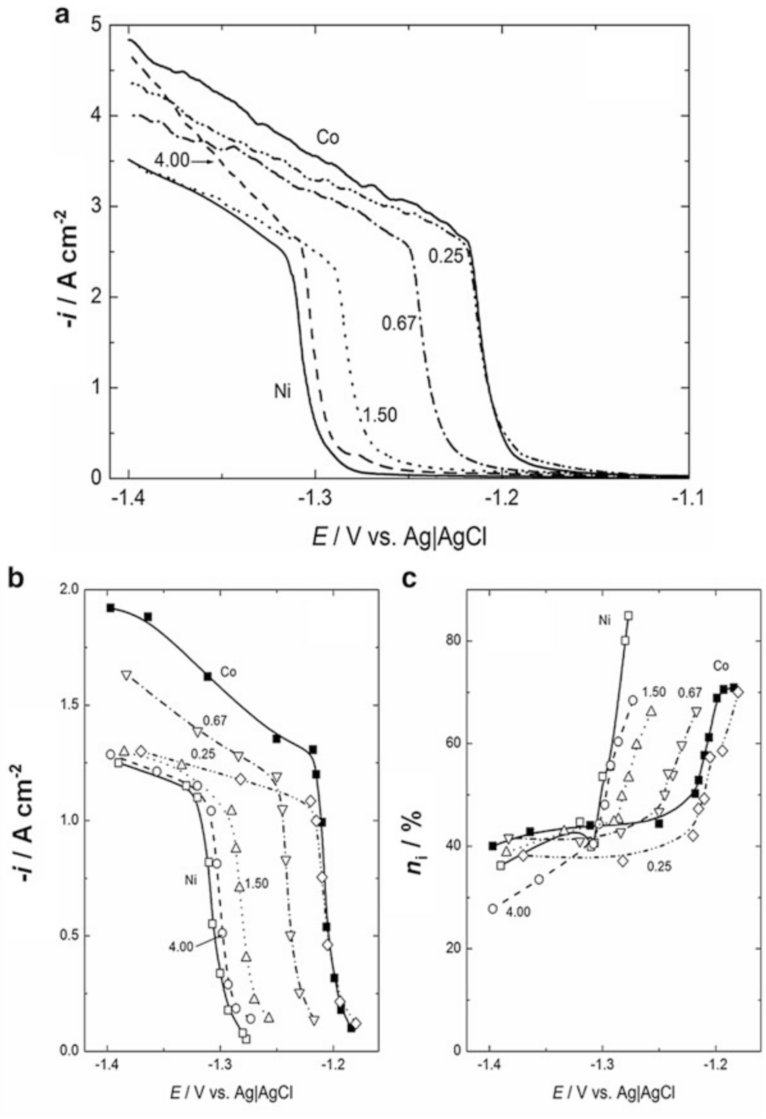

Fig. 8.6 (**a**) Polarization curves for the electrodeposition of cobalt (Co), nickel (Ni), and Co-Ni alloy powders after IR drop correction recorded for different Ni^{2+}/Co^{2+} ions ratios: 4.00, 1.50, 0.67, and 0.25 (marked in the figure). (**b**) The same polarization curves after hydrogen evolution current density subtraction. (**c**) Corresponding η_i vs. E curves for (**b**) (Reprinted from Ref. [1] with kind permission from Springer)

indicating more efficient process of powder formation in the chloride-supporting electrolyte. This statement is supported with the η_i vs. E curves presented in Fig. 8.6c, where the current efficiency for powder electrodeposition is much higher than that in the sulfate-supporting electrolyte (Fig. 8.1c).

8.2.1.4 The Morphology of the Co-Ni Alloy Powders Electrodeposited from the Chloride-Containing Supporting Electrolyte

In Figs. 8.7, 8.8, 8.9, and 8.10 are shown SEMs of Co-Ni alloy powders obtained from a solution containing different Ni^{2+}/Co^{2+} ions ratios. At the Ni^{2+}/Co^{2+} ions ratio of 4.00 (22 at.% Co in the powder), Fig. 8.7, two types of agglomerates are detected: cauliflower ones (a), varying in size between 60 and 100 μm, and bigger (varying in size between 200 and 400 μm), spongy ones (b), similar to the morphology of pure Ni powder. In the case of alloy, these two types of agglomerates are not equally distributed, but most of the agglomerates (over 80 %) are spongy-like agglomerates.

With increasing the content of Co^{2+} ions in the solution, as well as Co content in the powder (Ni^{2+}/Co^{2+} ions ratio of 1.50, 42 at.% Co in the powder), very few cauliflower-like agglomerates can be detected in the powder electrodeposit (Fig. 8.8a), being of the size of about 100 μm, while most of them are spongy-like

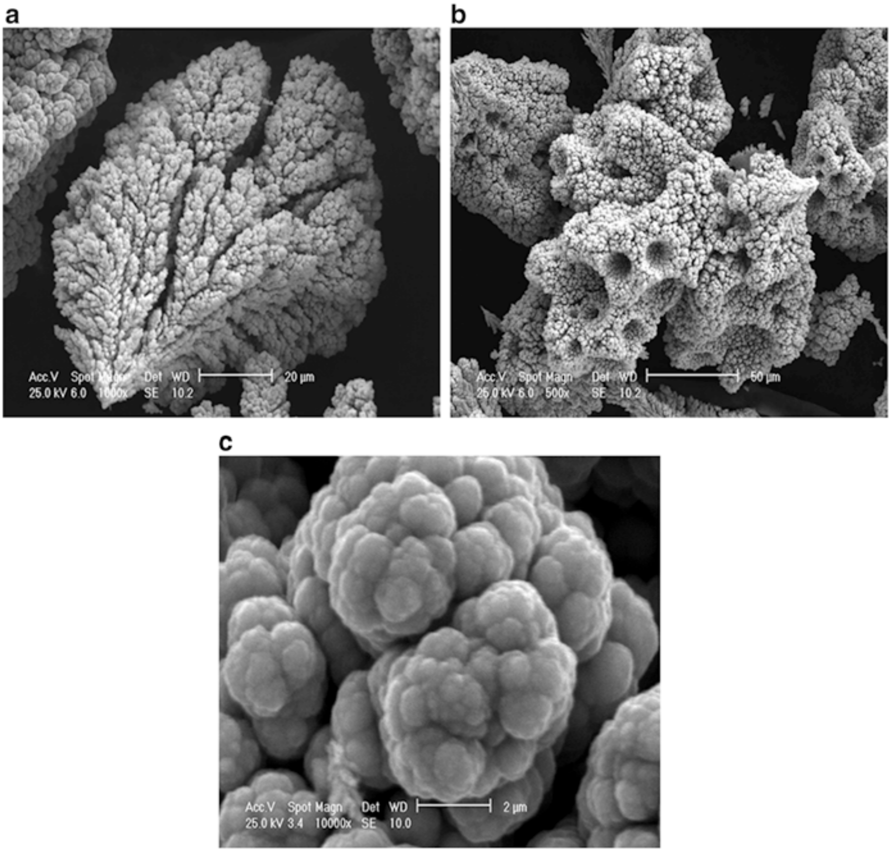

Fig. 8.7 Typical agglomerates detected in the powder electrodeposited at the $Ni^{2+}/Co^{2+} = 4.00$. (**a**) Cauliflower agglomerate, (**b**) Spongy agglomerate, (**c**) Top view of spongy agglomerates at higher magnification (Reprinted from Ref. [1] with kind permission from Springer)

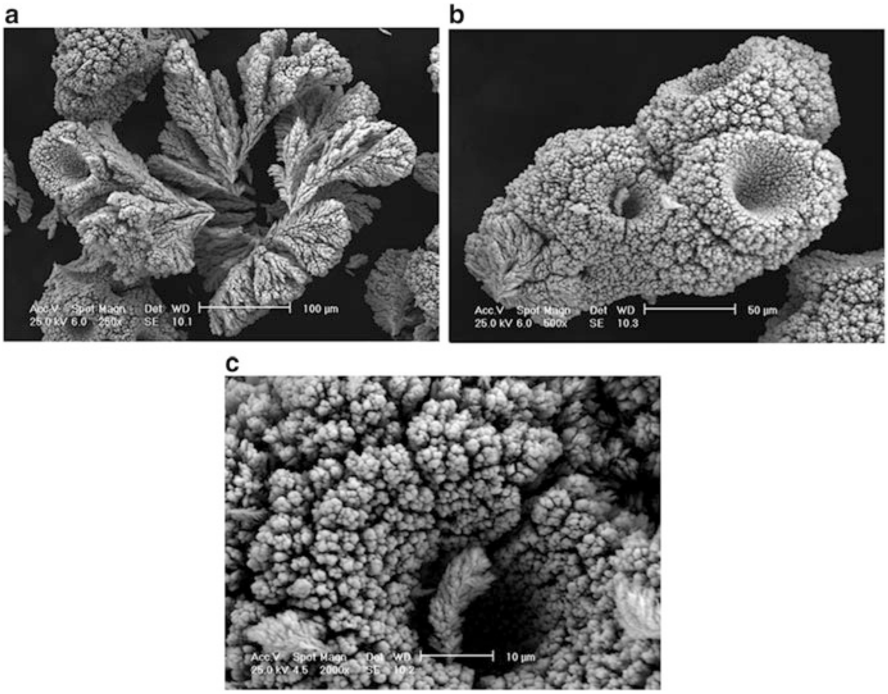

Fig. 8.8 Typical powder agglomerates detected in the powder electrodeposited at the $Ni^{2+}/Co^{2+} = 1.50$. (**a**) Few cauliflower-like agglomerates of about 100 μm, (**b**) Spongy-like agglomerates of about 200 μm, (**c**) Top view of spongy agglomerates at higher magnification (Reprinted from Ref. [1] with kind permission from Springer)

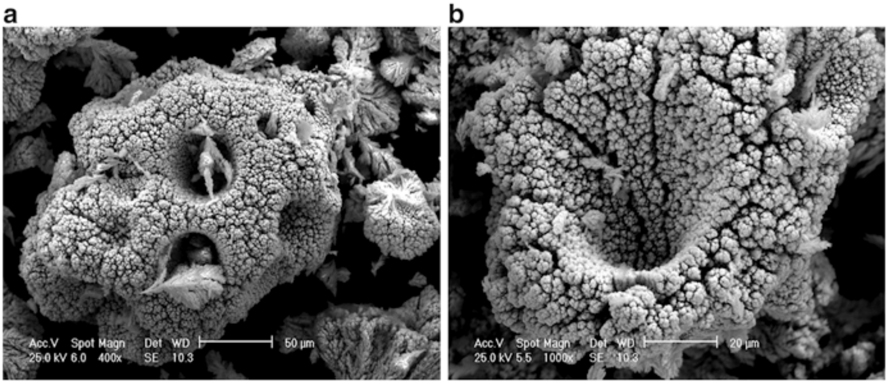

Fig. 8.9 Typical powder agglomerates detected in the powder electrodeposited at the $Ni^{2+}/Co^{2+} = 0.67$. (**a**) Narrow (cylindrical) cavities with fern-like dendrites on their bottom, (**b**) Cone-shaped cavities without fern-like dendrites on their bottom (Reprinted from Ref. [1] with kind permission from Springer)

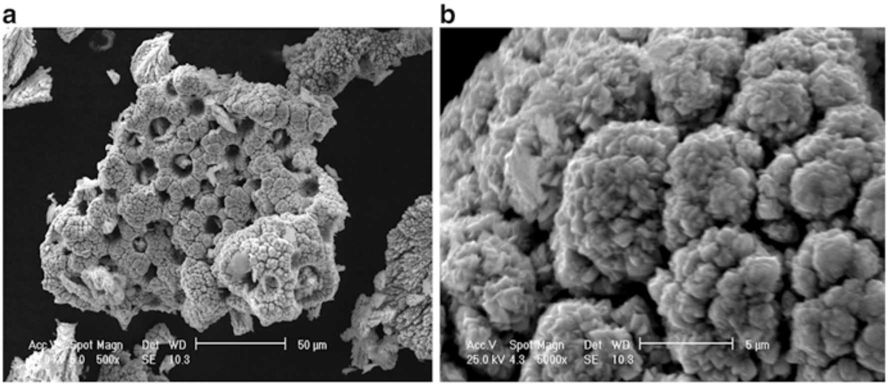

Fig. 8.10 Typical powder agglomerates detected in the powder electrodeposited at the $Ni^{2+}/Co^{2+} = 0.25$. (**a**) Typical spongy agglomerate, (**b**) Agglomerate with the presence of well-defined crystals on the cauliflower endings (Reprinted from Ref. [1] with kind permission from Springer)

ones of a bigger size of about 200 μm (Fig. 8.8b). It is characteristic for spongy agglomerates that two types of cavities could be detected on all powder agglomerates: narrow (cylindrical) cavities with fern-like dendrites formed at their bottom (Fig. 8.8c), indicating that before agglomerates detached from the electrode surface conditions of planar diffusion in the cavity were established causing formation of fern-like dendrites, and wider, cone-shaped cavities without fern-like dendrites on their bottom (Fig. 8.8a, b). It is most likely that the absence of fern-like dendrites at the bottom of cone-shaped cavities is the consequence of the fact that because of such a shape, with wide opening, no condition for planar diffusion in these cavities was established.

With further decrease of Ni^{2+}/Co^{2+} ions ratio to 0.67 (65 at.% Co in the powder), no cauliflower-like agglomerates are detected. All agglomerates are spongy-like, again with two types of cavities: narrow (cylindrical) ones with fern-like dendrites on their bottom (Fig. 8.9a) and cone-shaped ones (Fig. 8.9b) without fern-like dendrites on their bottom. The top surface of all agglomerates obtained from these three solutions is practically identical, being characterized by cauliflower nature, as shown in Fig. 8.7c.

At the lowest Ni^{2+}/Co^{2+} ions ratio of 0.25 (82 at.% Co in the powder), the same types of spongy agglomerates as ones obtained from the solution containing Ni^{2+}/Co^{2+} ions ratio of 0.67 are obtained (Fig. 8.10a). In this case, two types of spongy agglomerates, concerning the top surface of the agglomerates, are detected: agglomerates with flat noodle-like endings (Fig. 8.7c) and agglomerates with the presence of well-defined crystals on the cauliflower endings, as shown in Fig. 8.10b. It is most likely that the detachment of agglomerates shown in Fig. 8.10b occurred later than the detachment of agglomerates shown in Fig. 8.7c, allowing formation of a second layer of their growth to take place [1, 3]. Hence, in comparison with pure metal powders, agglomerates of alloy powders are characterized by the presence of two types of cavities: cylindrical ones with the fern-like dendrites on their bottom, indicating that hydrogen bubbles are liberated before the powder agglomerate detachment, and cone-shaped ones without fern-like dendrites on their bottom (because of the cavity shape, planar diffusion cannot be established in the cavity), detected at smaller powder agglomerates. The appearance of such cavity is most probably due to different (higher) rates of hydrogen bubble formation in this solution. Comparing results obtained in chloride-containing electrolyte with the results obtained in sulfate-containing electrolyte, the following remarks could be made: (1) polarization curves for hydrogen evolution in supporting electrolytes are different, with the one recorded in the chloride-containing supporting electrolyte being characterized with higher current densities, indicating faster hydrogen evolution in the presence of smaller anions (see Fig. 2.24, Ref. [17]); (2) correct polarization curves for pure metals and alloy powder electrodeposition are also characterized with higher current densities, as well as higher current efficiencies for powder electrodeposition, indicating faster and easier powder formation in chloride-containing electrolyte; (3) relatively similar morphologies of powder agglomerates are detected in both solutions, with the distribution of agglomerates being different in all cases. Characteristic feature of powder agglomerates obtained from chloride-containing electrolytes is the presence of cone-shaped cavities.

8.2.1.5 The Morphology of the Co-Ni Alloy Powders Electrodeposited from the Borate-Sulfate Containing Supporting Electrolyte

At the highest Ni^{2+}/Co^{2+} ions ratio in the solution ($Ni^{2+}/Co^{2+} = 1.00$, 55 at.% Co in the powder), all powder agglomerates possess 2D fern-like shape [7], varying in the size from about 100 μm to about 200 μm, as can be seen in Fig. 8.11 [1]. They are all practically two dimensional (Fig. 8.11a), although at higher magnification

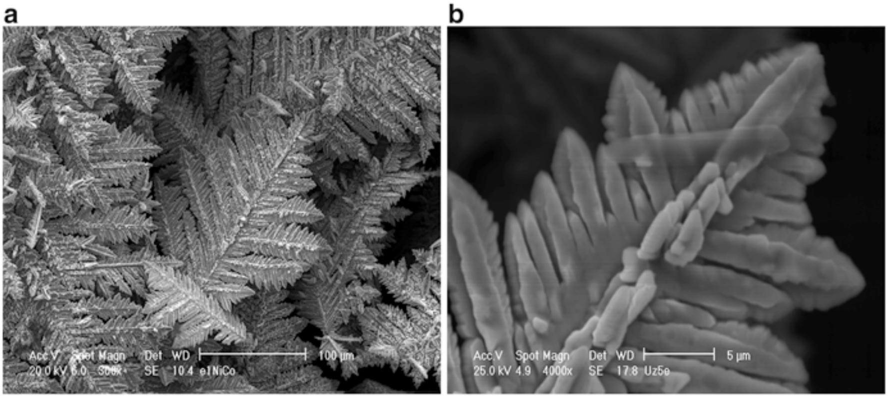

Fig. 8.11 Typical powder agglomerates detected in the powder electrodeposited at the $Ni^{2+}/Co^{2+} = 1.00$. (**a**) Agglomerates with 2D fern-like shape, (**b**) 2D fern-like agglomerate at higher magnification (Reprinted from Ref. [1] with kind permission from Springer)

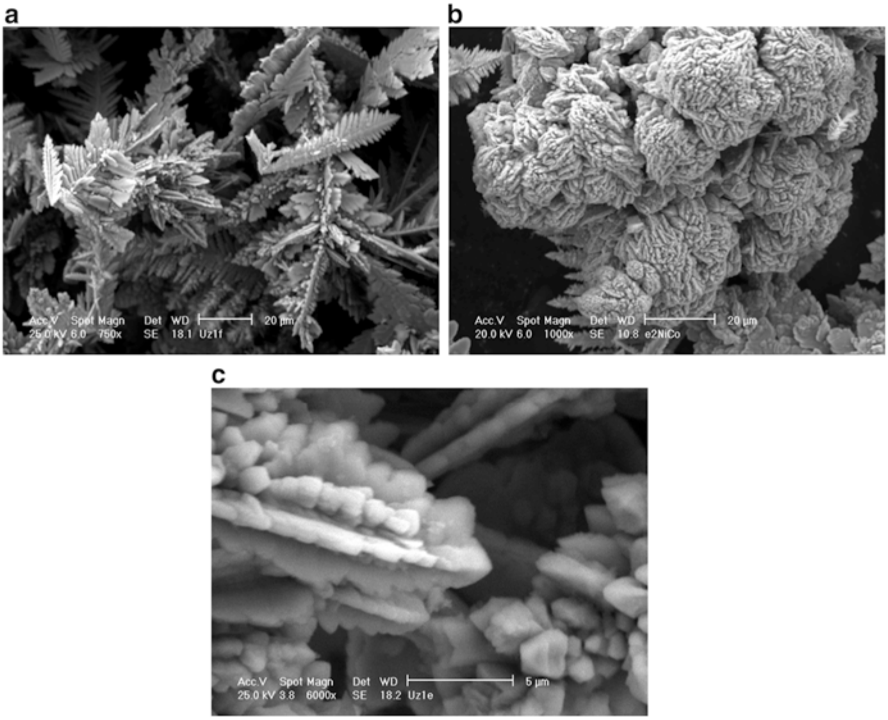

Fig. 8.12 Typical powder agglomerates detected in the powder electrodeposited at the $Ni^{2+}/Co^{2+} = 0.50$. (**a**) 2D fern-like agglomerates, (**b**) Agglomerates of the size of about 100 µm composed of a densely packed dendritic agglomerates, (**c**) Top view of dendritic agglomerates at higher magnification (Reprinted from Ref. [1] with kind permission from Springer)

(Fig. 8.11b) it can be seen that a third dimension of their growth also exists, but it seems that this is a practically two-dimensional layer-by-layer growth following original dendrite shape. It can also be seen that on the main branch of such dendrite, small dendritic agglomerates, growing in the direction normal to the layer-by-layer growth, could be detected (Fig. 8.11b).

With the decrease of the Ni^{2+}/Co^{2+} ions ratio in the solution (0.50), i.e., the increase of the Co content in the alloy powder (80 at.% Co in the powder), among 2D fern-like agglomerates of a smaller size than in a previous case (varying in the size between 50 and 100 µm – Fig. 8.12a), agglomerates of the size of about 100 µm composed of a densely packed dendritic agglomerates were detected, as can be seen in Fig. 8.12b. It is interesting to note that dendrites covering the surface of such agglomerates are not 2D fern-like type. As can be seen in Fig. 8.12c, they are branching in four directions, but they are more compact and branches are much smaller, as are the dendrites (about 10 µm long and about 2 µm wide).

With further decrease of the Ni^{2+}/Co^{2+} ions ratio in the solution (0.33, 83 at.% Co in the powder), compact agglomerates, typical for pure Co powder, could be clearly detected in the powder electrodeposit, as can be seen in Fig. 8.13a, together

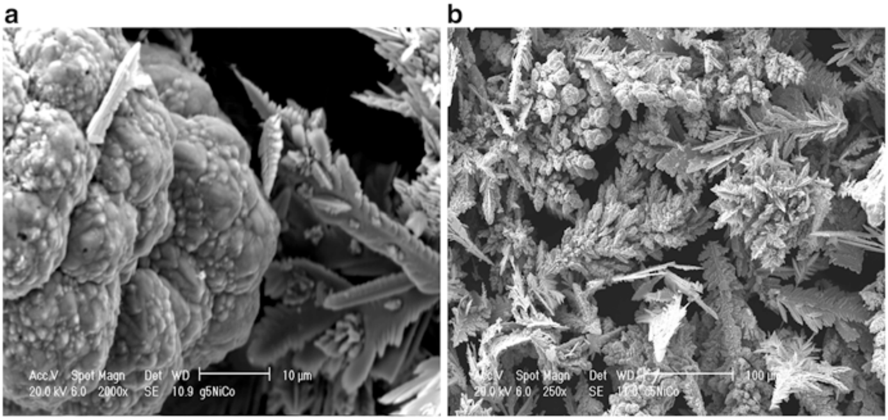

Fig. 8.13 Typical powder agglomerates detected in the powder electrodeposited at the $Ni^{2+}/Co^{2+} = 0.33$. (**a**) Compact agglomerates together with the 2D fern-like dendrites, (**b**) Densely packed 3D dendritic agglomerates (Reprinted from Ref. [1] with kind permission from Springer)

with the 2D fern-like dendrites. By the EDS analysis of compact agglomerates, it was confirmed that they do not represent pure Co particle, but the Co-Ni alloy, indicating that similar shapes of agglomerates characterize pure Co and Co-Ni alloy powder deposit. The presence of densely packed 3D dendritic agglomerates can also be seen in this powder, as shown in Fig. 8.13b. Again, these dendrites are more compact and smaller than those recorded on powder agglomerates electrodeposited at the Ni^{2+}/Co^{2+} ions ratio 0.50.

It is noteworthy that with the increase of the h.c.p. α-Co (100) phase in the powder electrodeposit and the decrease of the f.c.c. β-Ni (111) phase, the shape of dendrite agglomerates changes from typical 2D fern-like dendrites to 3D dendrites. This is in accordance with the statement [1] that in the presence of the (111) orientation (f.c.c. β-Ni (111) phase) 2D dendrite growth prevails (the highest intensity for f.c.c. β-Ni (111) phase is detected in sample electrodeposited at Ni^{2+}/Co^{2+} ions ratio 1.00). Such dendrites are denoted in the literature [1] as 2D{100} 60°, with the angle of 60° between the main tree of the dendrite and the branches. In order to explain the influence of other orientations (h.c.p. α-Co (100) etc.) on the growth of dendrites in the investigated powder and appearance of 3D dendrites in the powder deposit, additional experiments and more detailed analysis are needed.

8.2.2 Electrodeposited Fe-Ni Alloy Powders

Electrodeposition of Fe-Ni powders was performed in ammonium chloride–sodium citrate containing electrolyte of the composition 1 M $NH_4Cl + 0.2$ M $Na_3C_6H_5O_7$. Fe(III) and Fe(II) chloride and nickel chloride were used as sources of Fe^{2+} or Fe^{3+} and Ni^{2+} ions. Total concentration of cations was kept at 0.1 M. Four different

Ni/Fe concentration ratios were investigated: Ni/Fe = 9/1; Ni/Fe = 3/1; Ni/Fe = 1/1; and Ni/Fe = 1/3. In the case of Fe(III) ions, pH of the solution was adjusted to 4.5, while in the case of Fe(II) ions, pH of the solution was adjusted to 4.0. All solutions were made from analytical grade purity chemicals and distilled water by the following procedure: $Na_3C_6H_5O_7$ was first dissolved and the pH was adjusted to slightly higher value than desired by HCl; in the next step, metal (Fe(III), Fe(II), or Ni) salts were dissolved; finally, ammonium chloride was added and pH adjusted to the exact value. Concerning stability of solutions, it is well known that during the investigation, some Fe(II) become oxidized into Fe(III). This should be particularly pronounced during the electrodeposition of powders for 1 or 2 h. Taking into account that in all cases Fe(II) or Fe(III) made very stable complexes with citrate anions, no problems have been experienced in the case of polarization measurements (polarization curves were practically the same after 3–4 measurements), but for any case before each experiment, fresh solution was made and used for investigation as well as for powder electrodeposition [1, 8].

It should be mentioned here that an attempt was made to deposit Fe-Ni powders from the electrolytes of the same composition but of low pH 2. The powder agglomerates were successfully produced on the cathode, but immediately after detaching from the cathode surface, they started dissolving with gas evolution in all investigated electrolytes. Only in the case of very short time of electrolysis and removal of remained powder (which had not yet been dissolved) it was possible to obtain small amount of powder for further analysis. That was the reason why all experiments were performed in the solutions of pH 4.0 or 4.5, since in this solution powders were stable after electrodeposition.

From all solutions, Fe-Ni alloy powders were electrodeposited at a constant current density corresponding to the slightly lower value (i_{pd}) than the inflection point B (marked with (●)) on the polarization curves (see Fig. 8.14) [1, 8].

8.2.2.1 Polarization Curves for Fe-Ni Alloy Powder Electrodeposition from Chloride: Citrate-Supporting Electrolyte

The polarization curves corrected for IR drop for the processes of Fe, Ni, and Fe-Ni alloy powder electrodeposition from ammonium chloride–sodium citrate containing supporting electrolyte in the presence of Fe(II) and Ni(II) species are shown in Fig. 8.14. In the case of Fe(II) salts, polarization curve for iron electrodeposition (Fe) was placed at more positive potentials than that for nickel (Ni) as it is expected from the values of their reversible potentials. The polarization curves for Fe-Ni alloy powder electrodeposition are placed in between, and all of them were placed at more positive potentials than expected from the Ni/Fe ratio, indicating anomalous codeposition.

It was found that for the Fe(III) salt electrolytes, the current efficiency was very low, 1–2 % (polarization curves for powder electrodeposition (i_{tot}) and for hydrogen evolution (i_H) practically overlapped), and it was necessary to electrodeposit powders at least for 2 h in order to obtain amount of powder that could be used for

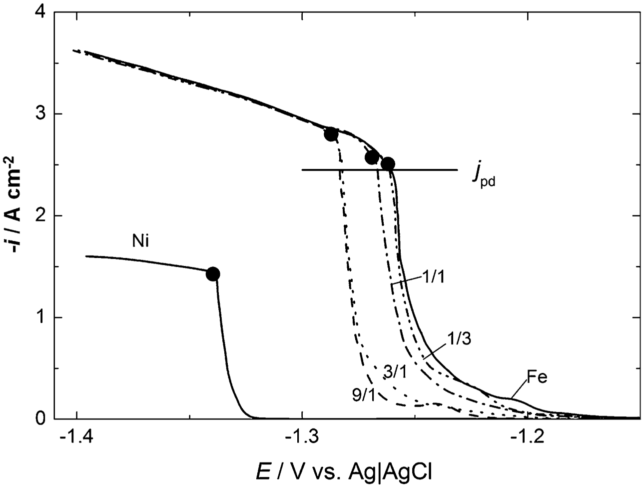

Fig. 8.14 Polarization curves for the electrodeposition of iron (Fe), nickel (Ni), and Fe-Ni alloy powders after IR drop correction recorded for different Ni/Fe ions ratios (9/1, 3/1, 1/1, and 1/3 (marked in the figure)), in the solution of Fe(II) and Ni(II) species (Reprinted from Ref. [1] with kind permission from Springer)

the morphology and composition analysis (SEM, EDS). In the case of Fe(II) salt electrolytes, current efficiency at the potentials more negative than the second inflection point (● in Fig. 8.14) varied between 8 % and 15 % depending on the Ni/Fe ratio, as shown in Fig. 8.15. The average values for the diffusion-limiting current densities for alloy powder electrodeposition were $i_{\text{Fe-Ni}} = -0.26$ A cm^{-2} for the ratio 1/3 and $i_{\text{Fe-Ni}} = -0.49$ A cm^{-2} for the ratio 9/1 [1, 8].

With the increase of iron concentration (as well as with the increase of the amount of iron in the powder – decrease of Ni/Fe ratio), the current efficiency for powder electrodeposition decreased, which is in accordance with the data obtained for compact Fe-Ni alloy electrodeposits [1, 18].

The polarization curves were recorded starting from the potential of −0.6 V vs. Ag|AgCl. By comparing polarization curves for Fe powder electrodeposition from Fe (III) (curve **a**) and Fe(II) (curve **b**) salts in ammonium chloride–sodium citrate electrolyte, shown in Fig. 8.16, certain cathodic current density (~ −2.5 mA cm^{-2}) has been detected already at the starting potential for curve **a** (inset of Fig. 8.16). This cathodic current density remained constant down to the potential of about −1.0 V versus Ag|AgCl, and it started rising at the same potential value at which the current density recorded in the presence of Fe(II) salt started to rise.

A low current efficiency for the Fe-Ni alloy powder electrodeposition from the solution containing Fe(III) salt is the consequence of the first step in the overall reaction being reduction of Fe(III) species into Fe(II) species, taking place at all potentials more negative than −0.2 V versus Ag|AgCl. Nevertheless, some experiments were performed in the solution of Fe(III) ions and the morphology of electrodeposited Fe-Ni alloy powders was investigated.

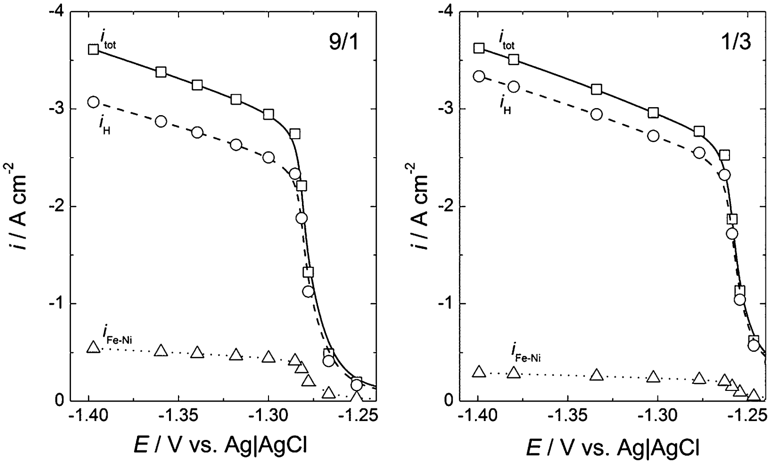

Fig. 8.15 Polarization curve for the Fe-Ni alloy powder electrodeposition (i_{tot}) (□), polarization curve for hydrogen evolution (i_H) (○), and polarization curve for Fe-Ni powder electrodeposition after subtraction of hydrogen evolution current ($i_{Fe\text{-}Ni}$) (Δ). The values of Ni/Fe ions ratios are marked in the figure (Reprinted from Ref. [1] with kind permission from Springer)

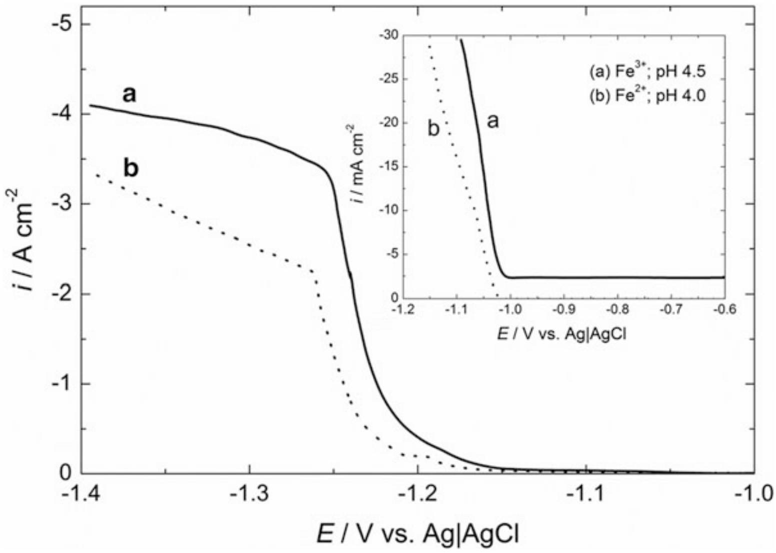

Fig. 8.16 The polarization curves for the electrodeposition of Fe powders from the electrolyte containing 0.1 M $FeCl_3$ + 0.2 M $Na_3C_6H_5O_7$ + 1 M NH_4Cl (**a**) and 0.1 M $FeCl_2$ + 0.2 M $Na_3C_6H_5O_7$ + 1 M NH_4Cl (**b**). Inset – the same polarization curves recorded at potentials more positive than −1.0 V versus Ag|AgCl (Reprinted from Ref. [1] with kind permission from Springer)

8.2.2.2 Morphology of the Fe-Ni Powders Electrodeposited from the Solutions Containing Fe(II) Species

The morphology of the Fe-Ni alloy powders electrodeposited at different Ni/Fe ratios is presented in Figs. 8.17, 8.18, 8.19, and 8.20. A common characteristic of all investigated Fe-Ni powders is the formation of big agglomerates (up to 500 μm).

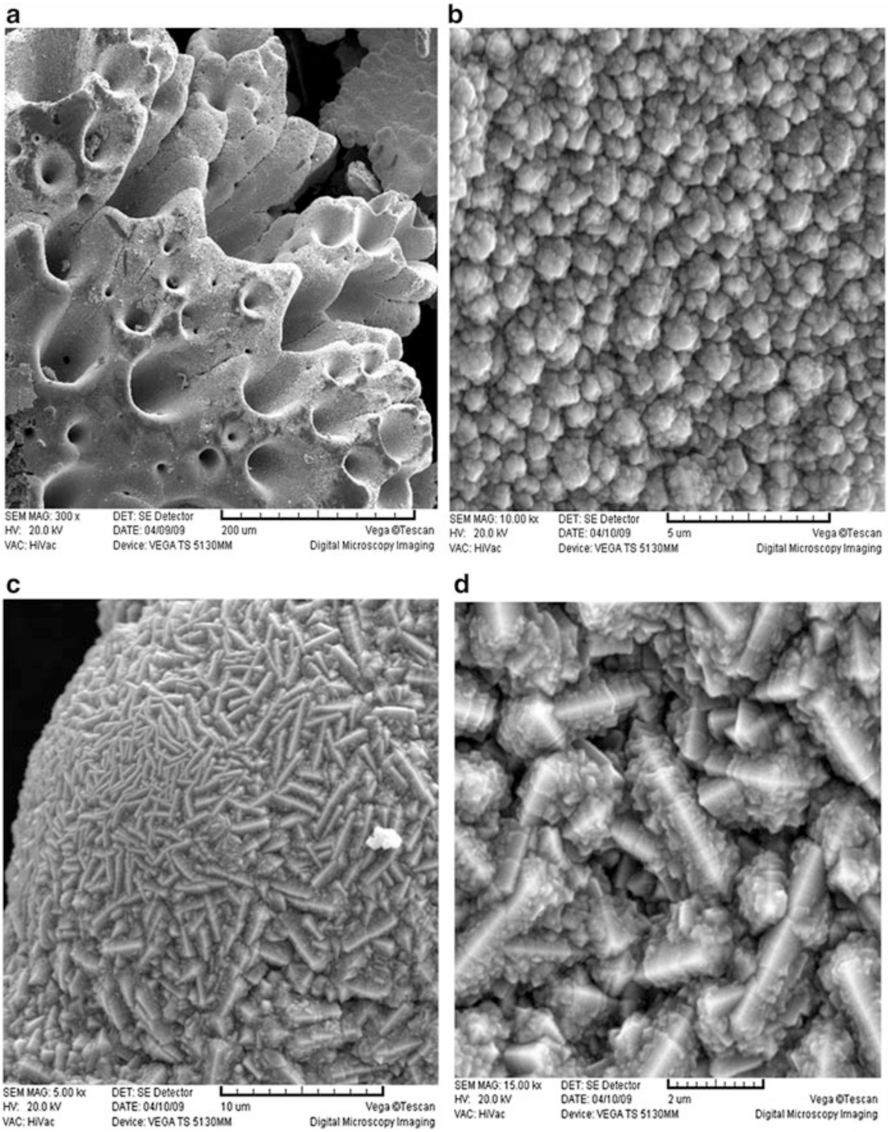

Fig. 8.17 Morphology of the Fe-Ni alloy powder electrodeposited at the Ni/Fe = 9/1. (**a**) Typical agglomerates with the large cone-shaped cavities and much smaller cylindrical cavities, (**b**) Pagoda-like crystals on nodular surfaces, (**c**) Crystals of the shape of elongated prism, (**d**) (**c**) at higher magnification (Reprinted from Ref. [1] with kind permission from Springer)

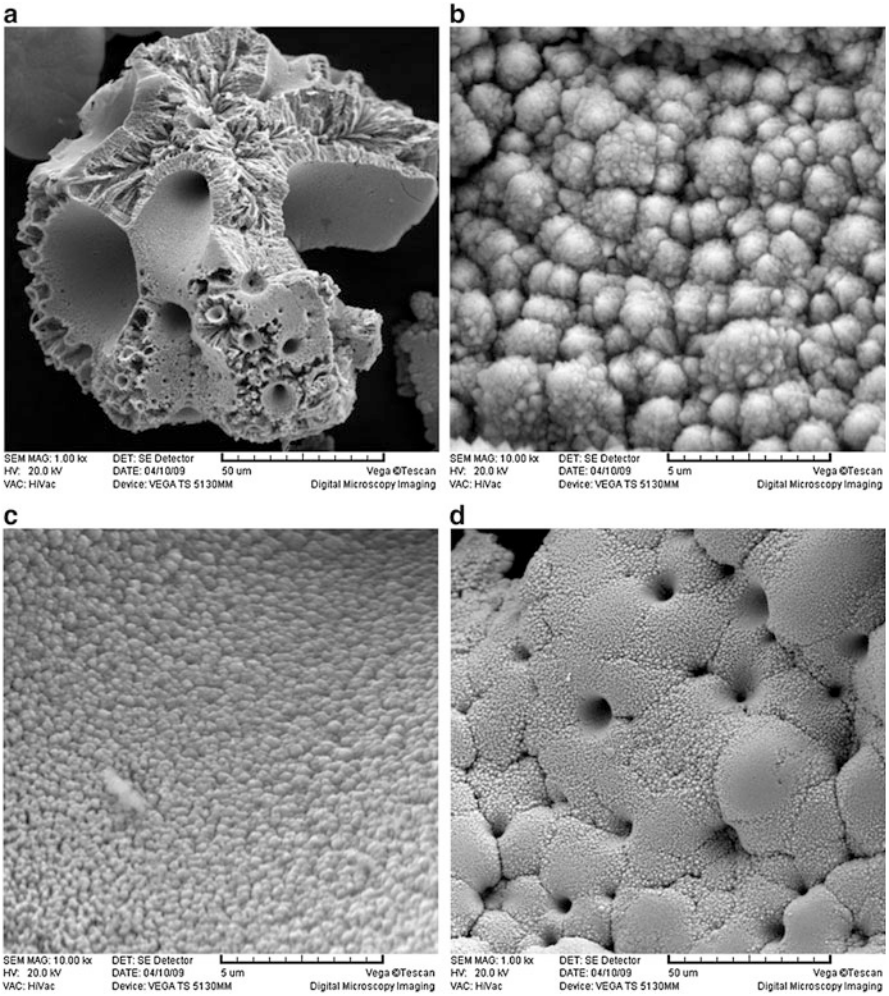

Fig. 8.18 Morphology of the Fe-Ni alloy powder electrodeposited at the Ni/Fe = 3/1 (Reprinted from Ref. [1] with kind permission from Springer)

Their surfaces are covered with large cone-shaped cavities, as well as with much smaller cylindrical cavities.

In Fig. 8.17 are presented typical agglomerates for Fe-Ni alloy powders electrodeposited at the Ni/Fe ratio 9/1. Large cone-shaped cavities and much smaller cylindrical cavities, corresponding to the places were hydrogen bubbles were formed, are clearly seen in Fig. 8.17a. Nodular surfaces are covered with two types of crystals: pagoda-like crystals (b) and crystals of the shape of elongated prism (c, d), indicating possible presence of different phases.

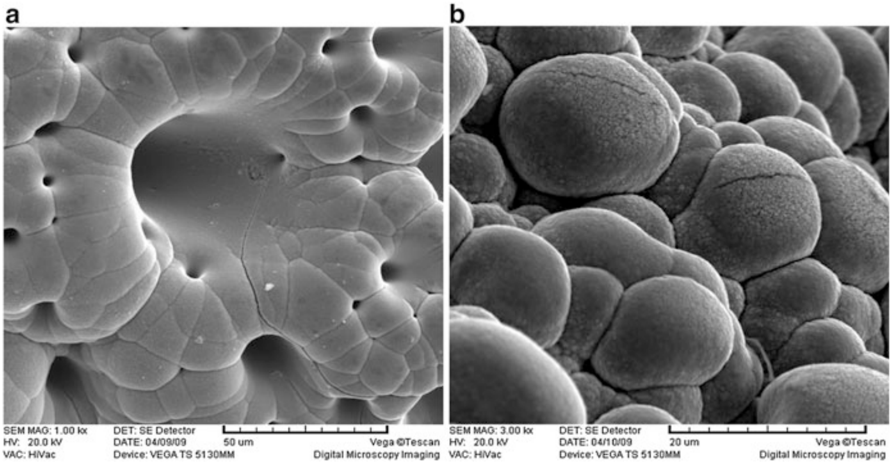

Fig. 8.19 Morphology of the Fe-Ni alloy powder electrodeposited at the Ni/Fe = 1/1. (**a**) Agglomerates with smooth surface of both types of cavities, (**b**) Top view of nodular endings (Reprinted from Ref. [1] with kind permission from Springer)

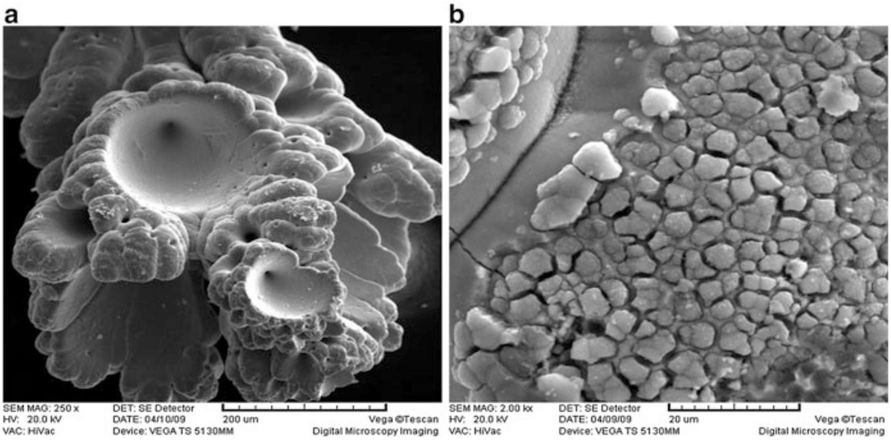

Fig. 8.20 Morphology of the Fe-Ni alloy powder electrodeposited at the Ni/Fe = 1/3. (**a**) Agglomerates with smooth surface of cavities, (**b**) Top view of nodular endings (Reprinted from Ref. [1] with kind permission from Springer)

Large cone-shaped cavities and much smaller cylindrical cavities are also present in the powder electrodeposited at Ni/Fe = 3/1 (Fig. 8.18a). Nodular surfaces (d) as well as the inside surface of cone-shaped cavities (c) are covered with spherical crystals (b).

Much smoother surface of both types of cavities and the nodular endings were obtained from the solution with Ni/Fe = 1/1 (Fig. 8.19).

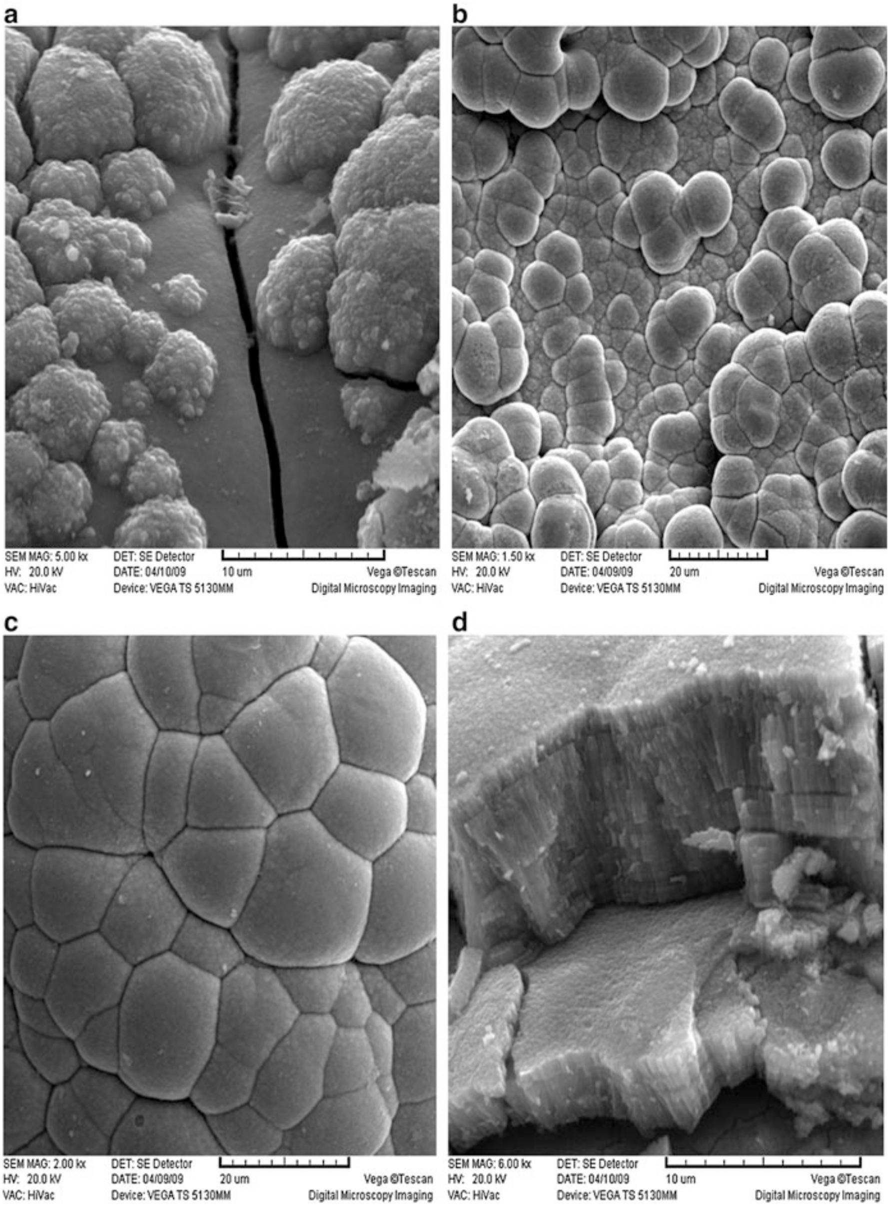

Fig. 8.21 Typical phases of the Fe-Ni powder growth. (**a**) Second generation of spherical grains, (**b**) Second generation of spherical grains on the compact surface, (**c**) Overlapping of spherical grains, (**d**) Layer-by-layer sticklike densely packed crystals of submicron dimensions (Reprinted from Ref. [1] with kind permission from Springer)

In the case of the highest content of iron in the powder (Ni/Fe = 1/3), a similar shape of cavities (Fig. 8.20a) was obtained as in Fig. 8.19a, while the surface of nodular endings was not smooth. On some parts of the agglomerate surface, new crystals were separated with the cracks, as shown in Fig. 8.20b.

Considering Figs. 8.17, 8.18, 8.19, and 8.20, it could be seen that on the compact surface of all agglomerates, smaller spherical (rounded) grains were formed (Figs. 8.21b–d and 8.19b). The formation of such spherical grains is typical for the electrodeposition of copper from acidic sulfate electrolytes under the conditions of activation–diffusion-controlled process [19]. Such mechanism has been explained for the electrodeposition of pure cobalt [17]. The development of spherical grains in the case of Fe-Ni electrodeposition is presented in Fig. 8.21. As can be seen in Fig. 8.21a, the second generation of spherical grains grow in all directions. On the compact surface, spherical grains are well defined (Fig. 8.21b), and since they are close to each other, they start to overlap. During the further growth, the overlapping of the diffusion zones formed over, and each spherical grain becomes more pronounced, producing practically flat surface of the agglomerates (Fig. 8.21c). It is interesting to note that the growth of compact agglomerates of spherical grains occurs through the formation of layer-by-layer sticklike densely packed crystals of submicron dimensions, as shown in Fig. 8.21d. Presented figures are in good agreement with already-given explanation for the electrodeposition of powders.

8.2.2.3 Morphology of the Fe-Ni Powder Electrodeposited from the Solutions Containing Fe(III) Species

The main characteristic of these powders is the presence of high number of both types of cavities on the surfaces of big agglomerates (up to 500 μm), as shown in Fig. 8.22. Taking into account that the current efficiency for the electrodeposition of these powders is only 1–2 %, massive hydrogen evolution must produce larger number of cavities than in previous cases. Also, one of the characteristics of these powders is the presence of several different types of crystals on the surface of agglomerates around the cavities, which are presented in Figs. 8.23 and 8.24. On the agglomerates, surfaces electrodeposited from the solutions with Ni/Fe = 9/1 and 3/1 mostly spherical crystals could be detected, as shown in Fig. 8.23a. At the same time, pagoda-like crystals (b) have been detected on a certain, not negligible, number of agglomerates.

Particularly interesting are crystals of the shape of pagoda. Such crystals were detected in the Fe-Ni powder synthesized in high yield by a simple and facile hydrothermal method without the presence of surfactants [1, 19]. According to this investigation, $FeNi_3$ {111} single crystals were formed during the described procedure. The products obtained at 120 °C were mixture of $FeNi_3$ and Fe-Ni hydroxides composed of monodispersed microspheres (probably spheres presented in Fig. 8.23a). With the increase of temperature to 140 °C, these microspheres became micropagodas very similar to those shown in Fig. 8.23b. At higher temperatures

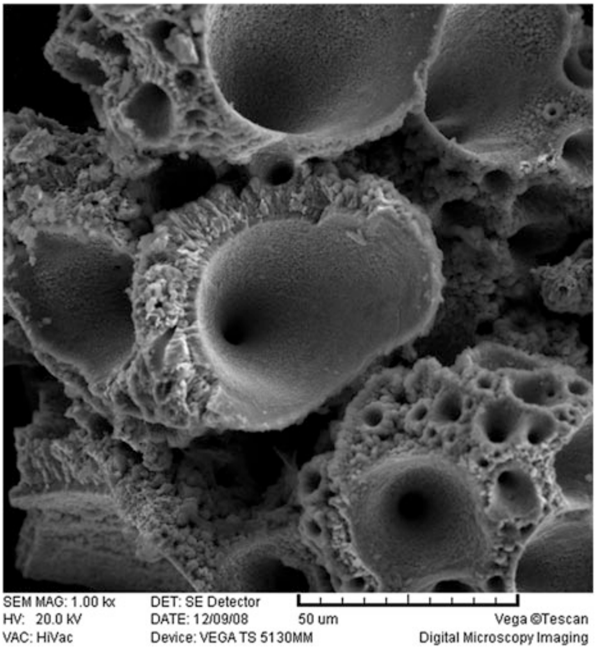

Fig. 8.22 Typical distribution of cavities on the surface of the Fe-Ni alloy powder agglomerates electrodeposited from the solution containing Fe(III) species (Reprinted from Ref. [1] with kind permission from Springer)

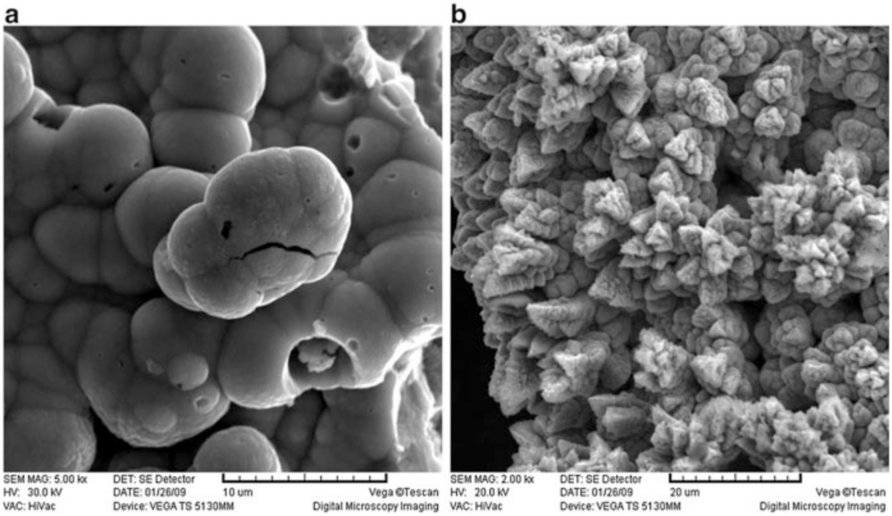

Fig. 8.23 Crystals formed on the surface of the Fe-Ni alloy powder agglomerates electrodeposited from the solution with Ni/Fe = 9/1 (Reprinted from Ref. [1] with kind permission from Springer)

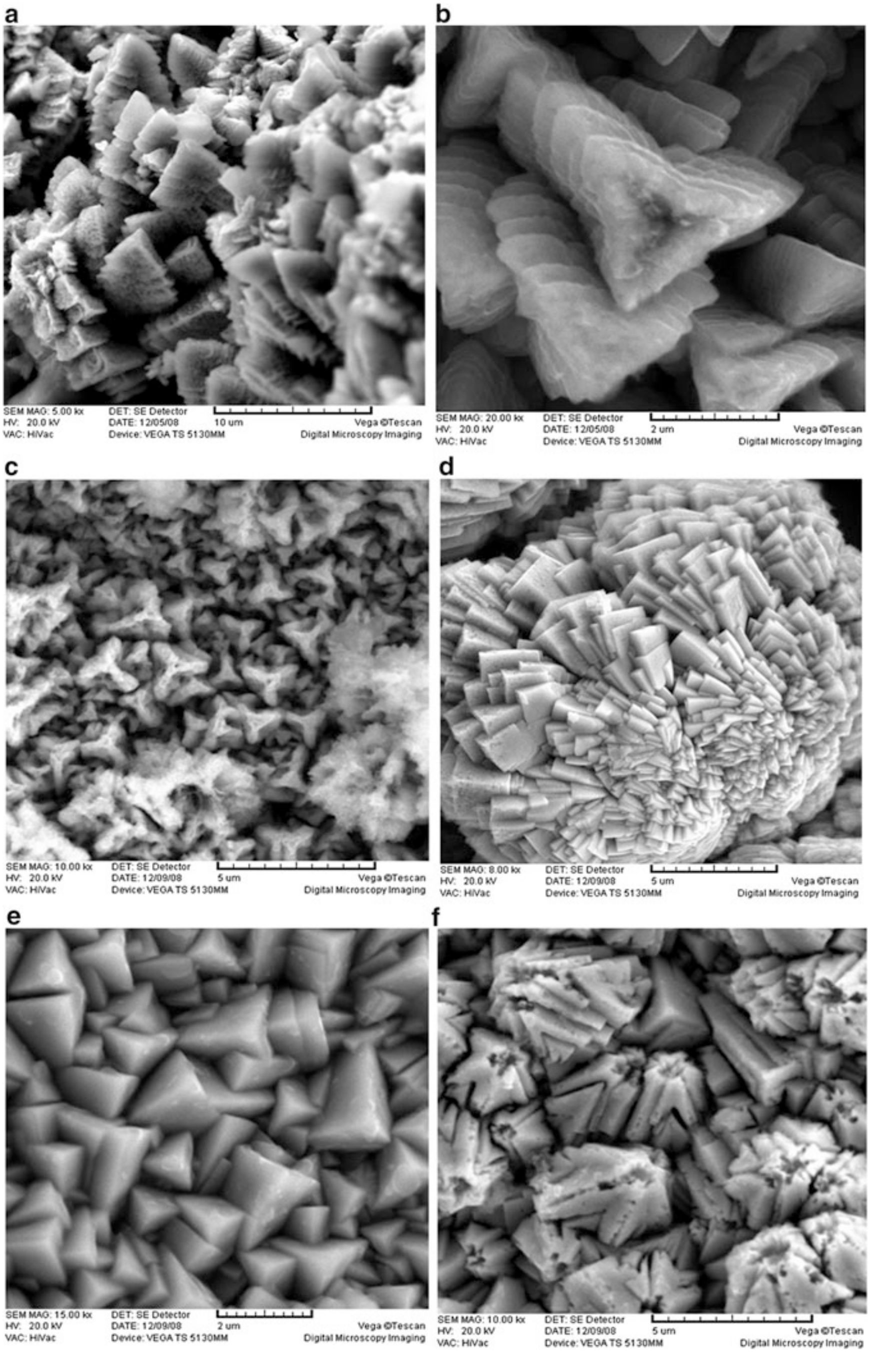

Fig. 8.24 Crystals formed on the surface of the Fe-Ni alloy powder agglomerates electrodeposited from the solution with Ni/Fe < 1 (Reprinted from Ref. [1] with kind permission from Springer)

(180 °C), these agglomerates transformed into perfect 3D $FeNi_3$ dendritic superstructures in certain directions [1, 19]. Hence, comparing the crystals presented in Fig. 8.23b with those obtained by hydrothermal method [1, 19], it seems reasonable to ascribe them to the $FeNi_3$ {111} single crystals (there is also an indication for the existence of $FeNi_3$ phase in electrodeposited powder – see XRD analysis presented in Fig. 28 of Ref. [1]).

As the amount of iron increases in the powders (above 50 at.%), the number of different crystals detected on the agglomerate surfaces also increases. In the powders electrodeposited from the solutions with Ni/Fe = 1/3, a very small amount of agglomerates is covered with spherical crystals, while most of them are characterized with the presence of several different shapes of crystals. These crystals are presented in Fig. 8.24a–f. It is quite difficult to explain the reasons for their appearance, since so many different phases do not exist in the Fe-Ni system and the only reasonable explanations could be that these crystals represent some superstructures formed under massive hydrogen evolution. Their shapes could be defined as follows: (a) Christmas tree-like crystals, (b) triangle-like crystals growing layer by layer, (c) propeller-like crystals, (d) plate-like crystals, (e) tetrahedral crystals, and (f) traversed polyhedron.

8.3 Induced Codeposition of Alloy Powders

8.3.1 *Electrodeposited Mo-Ni-O Powders*

The Mo-Ni-O powders were electrodeposited from two supporting electrolytes, as in the case of Co-Ni system: 1 M $NH_4Cl + 0.7$ M NH_4OH and 1 M $(NH_4)_2SO_4 + 0.7$ M NH_4OH, with the pH of the solutions being 9.0.

8.3.1.1 Polarization Curves in Chloride-Containing Electrolytes

Three different electrolytes were used for the investigations: 0.1 M $NiCl_2 + 1$ M $NH_4Cl + 0.7$ M $NH_4OH + x$ M Na_2MoO_4, with x being 0.05 M, 0.1 M, and 0.3 M, respectively. In such a way, the Ni/Mo ion concentration ratio was 1/0.5, 1/1, and 1/3. All powders for microstructure, composition, and phase composition analysis were electrodeposited at the limiting current density (position of the inflection point B on the polarization curves; see Fig. 8.25). In all cases, small amount of the rough compact electrodeposit (necessary for powder formation) remained on the glassy carbon surface, and only powder agglomerates detached from the cathode surface were analyzed.

The polarization curves are presented in Fig. 8.25. As can be seen, the polarization curves characterized by two inflection points (Fig. 8.25a), as in all previous cases, were obtained. It is important to note that the potential of the beginning of

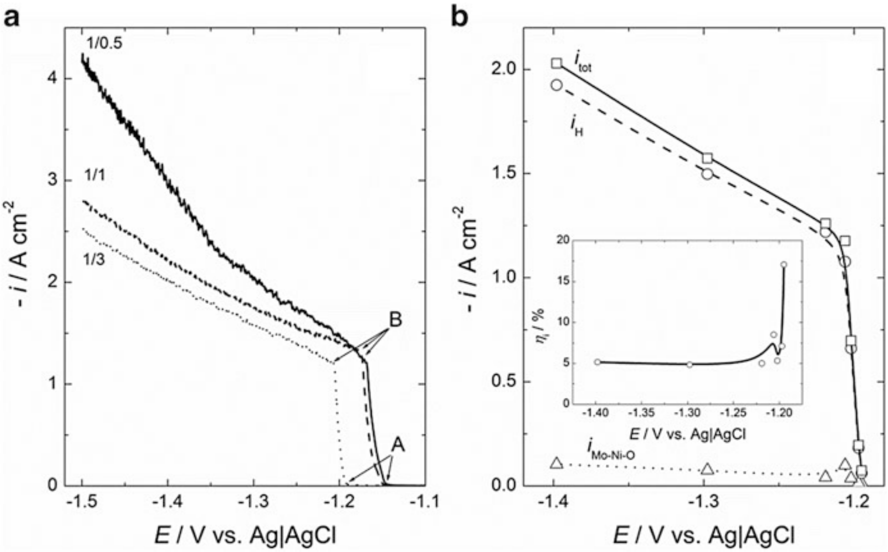

Fig. 8.25 (**a**) Polarization curves in chloride-containing electrolytes for different Ni/Mo ratios (marked in the figure). (**b**) Polarization curve for powder electrodeposition and hydrogen evolution (i_{tot}), polarization curve for hydrogen evolution (i_H), and polarization curve for powder electrodeposition after subtraction of the current density for hydrogen evolution ($i_{\text{Mo-Ni-O}}$). Inset: current efficiency for Mo-Ni-O powder electrodeposition (η_i) as a function of potential (Reprinted from Ref. [1] with kind permission from Springer)

alloy electrodeposition (A) becomes more negative with the increase of molybdate ion concentration (with the decrease of Ni/Mo ratio), as it could be expected, since the potential of the Mo electrodeposition is much more negative than that of Ni [13]. At the same time, electrodeposition of Mo can only take place in the presence of Ni (induced codeposition [13]). Taking into account that the concentration of Ni $^{2+}$ ions was constant, it is quite reasonable that the value of current density of the inflection point B did not change with changing Ni/Mo ion concentration ratio (being about -1.2 A cm^{-2}).

It should also be mentioned that the current efficiency for alloy electrodeposition in all cases was very low, about 5 %. This could be seen in the inset of Fig. 8.25b for the Ni/Mo ratio 1/3, where the η_i vs. E changes from 17 to 5 % in the region of sharp increase of current density, while at the potentials more negative than the second inflection point (B), the value of η_i is constant, being about 5 % [1, 14].

8.3.1.2 Polarization Curves in Sulfate-Containing Electrolytes

Three different electrolytes were used for the investigations: 0.1 M $NiSO_4 + 1$ M $(NH_4)_2SO_4 + 0.7$ M $NH_4OH + x$ M Na_2MoO_4, with x being 0.03 M, 0.1 M, and

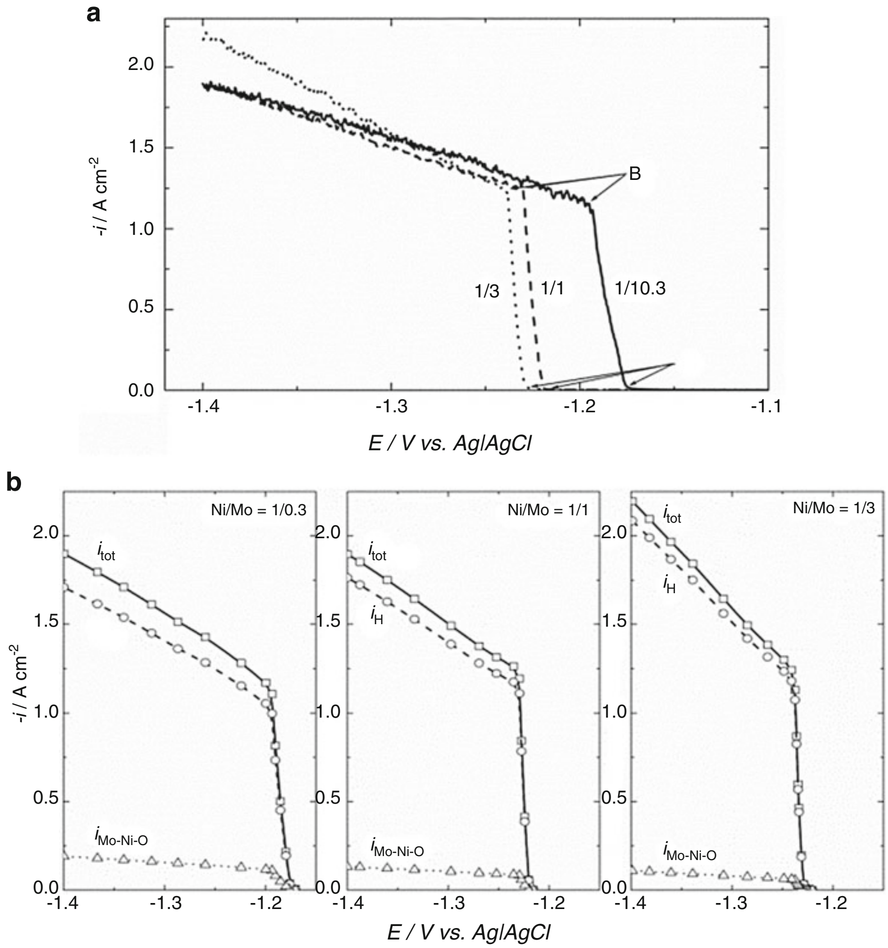

Fig. 8.26 (**a**) Polarization curves in sulfate-containing electrolytes for different Ni/Mo ratios (marked in the figure). (**b**) Polarization curves for powder electrodeposition and hydrogen evolution (i_{tot}), polarization curves for hydrogen evolution (i_H), and polarization curves for powder electrodeposition after subtraction of the current density for hydrogen evolution ($i_{Mo\text{-}Ni\text{-}O}$) (Reprinted from Ref. [1] with kind permission from Springer)

0.3 M, respectively. As in the case of chloride-containing supporting electrolytes, the Ni/Mo ion concentration ratio was 1/0.3, 1/1, and 1/3. The polarization curves recorded in the solution containing sulfate ions are presented in Fig. 8.26. In this case, all polarization curves are moved to slightly more cathodic potentials, indicating higher overvoltage for the process of Mo-Ni-O alloy electrodeposition in the presence of sulfate ions (Fig. 8.26a). At the same time, the total current densities in the range of potentials more negative than the inflection point (B) are smaller and the slopes of their changes are smaller in comparison with those recorded for chloride electrolyte (Fig. 8.25a). As well as in the case of chloride electrolyte, the potential of the beginning of alloy deposition (A) becomes more negative with the increase of molybdate ion concentration (with the decrease of Ni/Mo ratio). As shown in Fig. 8.26b, the current efficiency for alloy deposition is sensitive to the Ni/Mo ions ratio: for Ni/Mo = 1/0.3, $\eta_i = 10$ %, for Ni/Mo = 1/1, $\eta_i = 7$ %, and for Ni/Mo = 1/3, $\eta_i = 5$ % (all η_i values correspond to the potentials more negative than the second inflection point (B) [1, 15].

8.3.1.3 Morphology of Mo-Ni-O Powders Electrodeposited from Chloride-Containing Electrolytes

The morphology of powder agglomerates electrodeposited onto glassy carbon electrode from electrolytes with different Ni/Mo ions concentration ratios (1/0.5, 1/1, and 1/3, samples 1, 2, and 3, respectively) are shown in Figs. 8.27 and 8.28, respectively. For the highest Ni/Mo ratio of 1/0.5 (Fig. 8.27), size of the agglomerates varies in the range of about 2–50 μm. At the same time, sharp edges could be detected on top of the surfaces of all agglomerates, indicating crystallinity of electrodeposited powder (Fig. 8.27b) [1, 14].

With the decrease of the Ni/Mo ratio (1/1), cauliflower-type agglomerates, Fig. 8.28a, b, characterized with spherical edges (Fig. 8.28c) and the presence of cracks, were obtained. Their size is much higher than that of the powder particles electrodeposited at the 1/0.5 ratio, varying in the range of about 50–500 μm. In the case of Ni/Mo ratio of 1/3 (Fig. 8.28d), flat and thin parts of the powder,

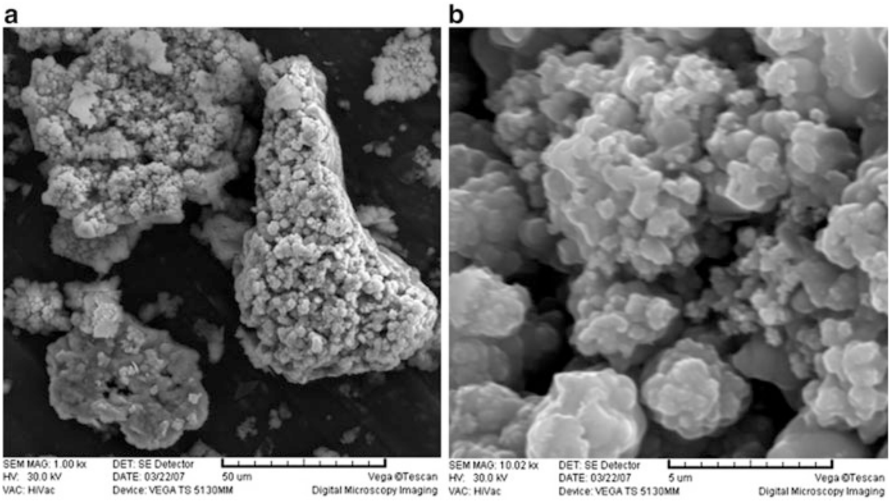

Fig. 8.27 Typical agglomerates for the Mo-Ni-O powders electrodeposited at the Ni/Mo = 1/0.5. (**a**) Agglomerates of the size in the range of about 2–50 μm, (**b**) Top view of sharp edges at the surfaces of agglomerates (Reprinted from Ref. [1] with kind permission from Springer)

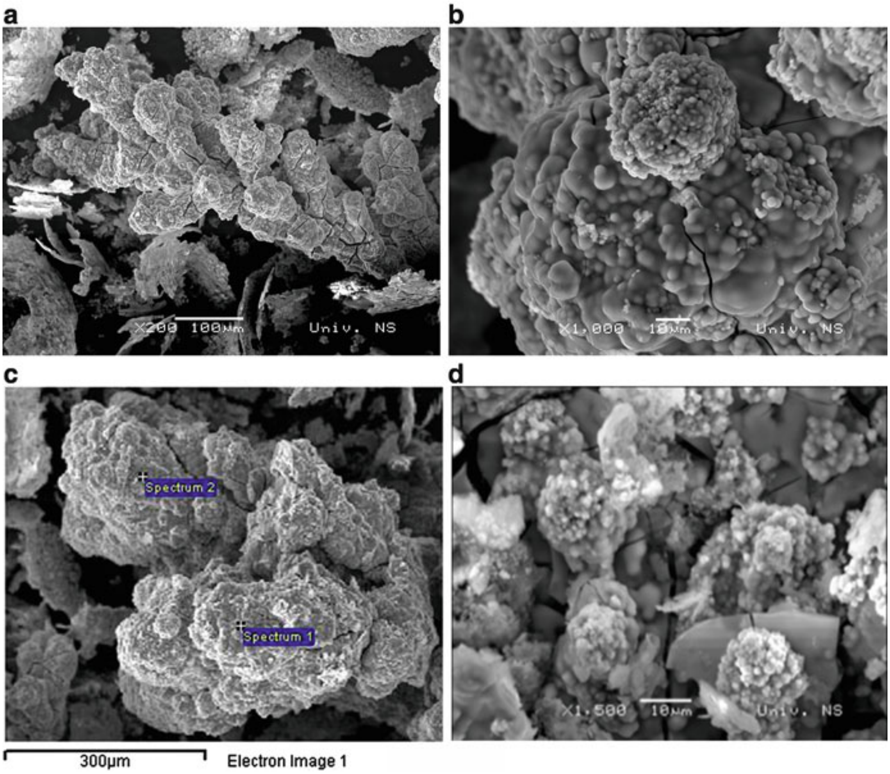

Fig. 8.28 (**a**–**c**) Typical particles for the Mo-Ni-O powders electrodeposited at the Ni/Mo = 1/1. (**d**) Typical particles for the Mo-Ni-O powders electrodeposited at the Ni/Mo = 1/3 (Reprinted from Ref. [1] with kind permission from Springer)

corresponding most likely to the compact electrodeposit, were covered with spherical agglomerates, while the cracks are more pronounced. The appearance of a large number of cracks is the result of high tensile stresses present in the powder and the hydrogen evolution [20]. According to the presented results, it is obvious that the crystallinity of the particles becomes less pronounced with the increase of molybdate ions in the electrolyte, influencing at the same time the morphology of electrodeposited powder particles.

8.3.1.4 Morphology of Mo-Ni-O Powders Electrodeposited from Sulfate-Containing Electrolytes

The morphology of powder particles electrodeposited from electrolytes with different Ni/Mo ion concentration ratios (1/0.3, 1/1, and 1/3) is shown in Figs. 8.29, 8.30, and 8.31. For the Ni/Mo ratio, 1/0.3 typical spongy particles were detected

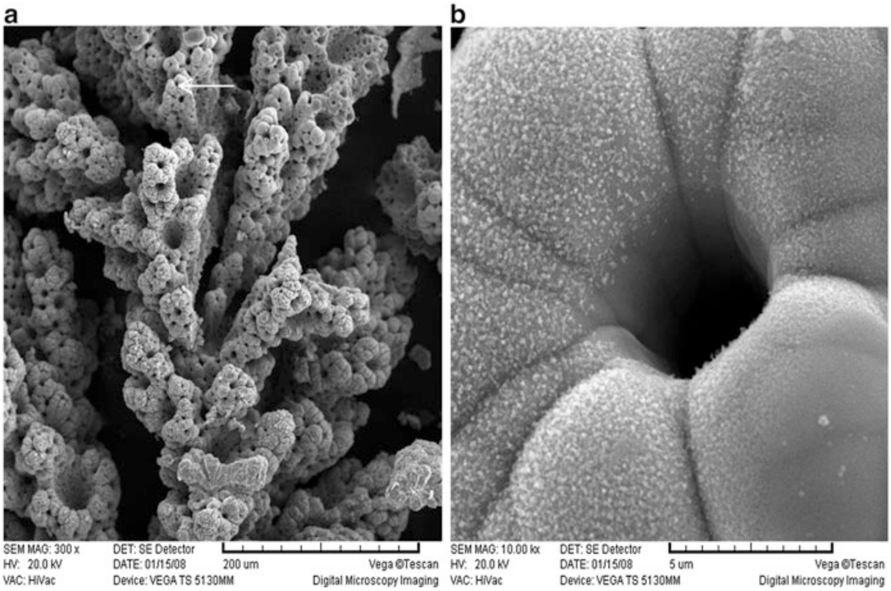

Fig. 8.29 (**a**) Typical spongy particles electrodeposited at the Ni/Mo = 1/0.3. (**b**) Cavity marked with *arrow* in (**a**) at higher magnification (Reprinted from Ref. [1] with kind permission from Springer)

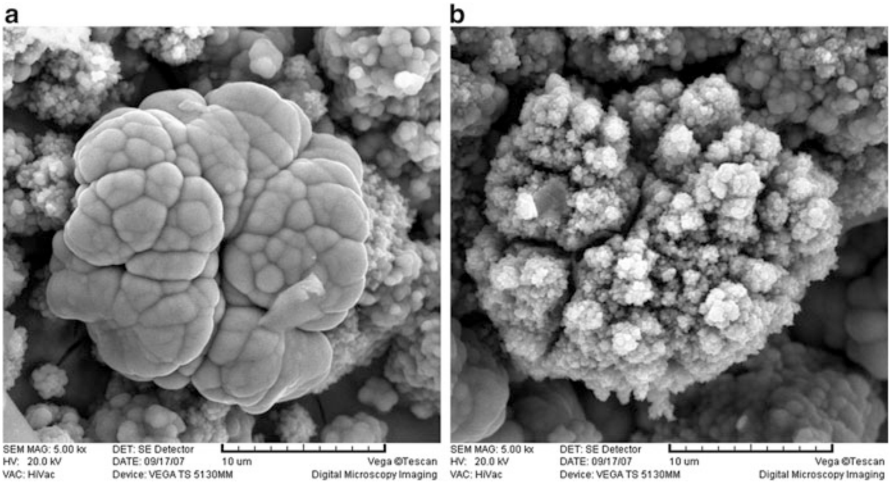

Fig. 8.30 Typical spongy particles electrodeposited at the Ni/Mo = 1/1 (Reprinted from Ref. [1] with kind permission from Springer)

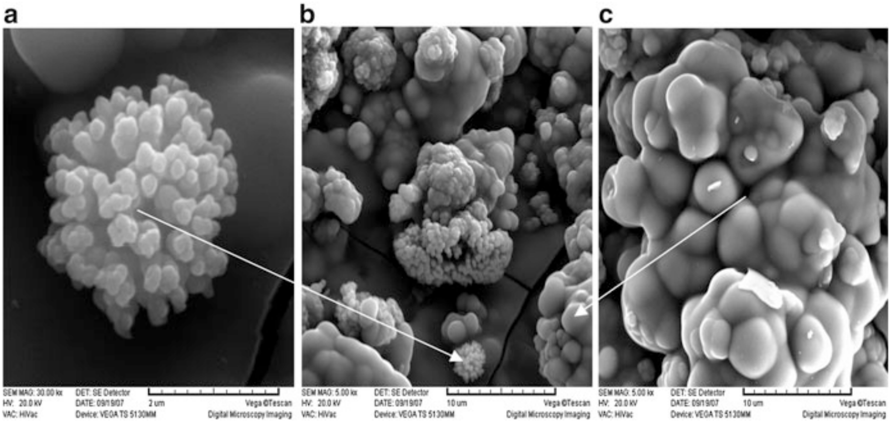

Fig. 8.31 (**b**) Typical powder electrodeposited at the Ni/Mo = 1/3. (**a**) Agglomerate with dendritic surface marked with the arrow in (**b**). (**c**) Agglomerate with flat surface marked with the arrow in (**b**) (Reprinted from Ref. [1] with kind permission from Springer)

(Fig. 8.29a). Characteristic of these particles is very flat surface around the holes, as shown in Fig. 8.29b.

With the decrease of the Ni/Mo ratio (1/1), two types of particles were obtained, as shown in Fig. 8.30. Both are spherical (rounded), one with flat edges (a) and another one with rough endings on top of the surface (b). Taking into account our previous investigations of alloy powder morphology [1, 3–6], this is not unexpected. Since the growth of powder particles is characterized by the presence of two or more growth zones, it appears that spherical particles with flat edges have been detached from the electrode surface before the beginning of a growth of new zone, while the particles with rough endings have been detached after the beginning of the growth of new crystals. It should be noted (not shown in this figure) that some particles were characterized by the presence of cracks.

In the case of Ni/Mo ratio of 1/3 (powder with the highest amount of molybdenum), a completely different morphology was detected, as shown in Fig. 8.31. The powder is composed of flat and thin parts with pronounced cracks, corresponding most likely to the compact electrodeposit, and spherical agglomerates growing on top of the flat electrodeposit (b). The surfaces of these agglomerates are either dendritic (a) or flat (c).

8.3.1.5 The Results of TEM Analysis of Mo-Ni-O Powders Electrodeposited from Sulfate Electrolyte

The TEM analysis was performed on two Mo-Ni-O powders: Ni-rich (Ni/Mo = 1/0.3) and Mo-rich (Ni/Mo = 1/3) powders. The common characteristic of both powders is the presence of amorphous and crystalline particles [1, 16].

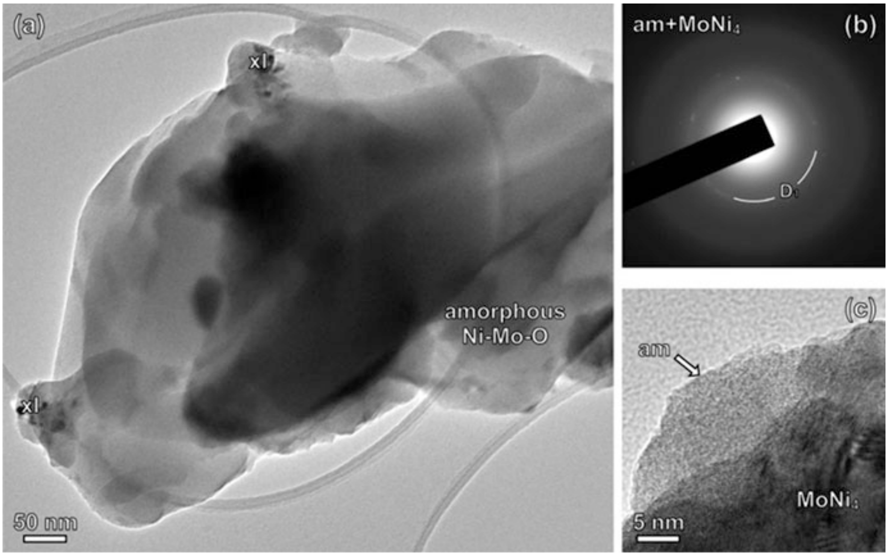

Fig. 8.32 (**a**) TEM image of the amorphous Mo-Ni-O particle detected in the powder electrodeposited at the Ni/Mo ratio 1/0.3. (**b**) SAED pattern recorded from this area (**a**) shows predominantly amorphous material (am) with weak reflections corresponding to $MoNi_4$ nanocrystals (x1). (**c**) High magnification of amorphous Mo-Ni-O particle with $MoNi_4$ nanocrystals (Reprinted from Ref. [1] with kind permission from Springer)

The TEM Analysis of Electrodeposited Ni-Rich Mo-Ni-O Powders

The specimen is composed of large amorphous clusters containing nanosized crystalline particles. Fig. 8.32 shows a TEM image of an amorphous particle (a) and the corresponding SAED pattern (b). Diffuse diffraction rings clearly indicate amorphous character of this powder particle. Weak spots in the diffraction pattern correspond to the {211} reflections of fine $MoNi_4$ nanoparticles (JCPDF # 65–1533) [21], shown in the close-up in Fig. 8.32c. In the crystalline parts of the Ni-rich powder, the following phases were detected: NiO, MoO_3, and $MoNi_4$, in form of idiomorphic crystallites measuring up to 70 nm in diameter. Figure 8.33 shows a cluster of well-crystallized nanoparticles. The SAED pattern (shown in Fig. 8.33b) from these clusters best corresponds to the monoclinic MoO_3 phase (JCPDF # 89–1554) [22], or one of its structural variants, depending on the position in the sample. Typical morphology of euhedral MoO_3 crystals is shown in Fig. 8.33a and on the close-up in Fig. 8.33c. Most of the crystals are tabular on {200}. The strongest SAED diffraction rings in the pattern correspond to $D_1 = \{200\}$, $D_2 = \{211\}$, $D_3 = \{220\}$, $D_4 = \{022\}$. In the Ni-rich areas of the sample, we observe crystalline $MoNi_4$ and NiO. $MoNi_4$ appears in form of irregularly intergrown grains measuring up to 10 nm in average.

An area of prevailing $MoNi_4$ composition is shown in Fig. 8.34a, with corresponding SAED pattern in Fig. 8.34b. The strongest reflections were indexed

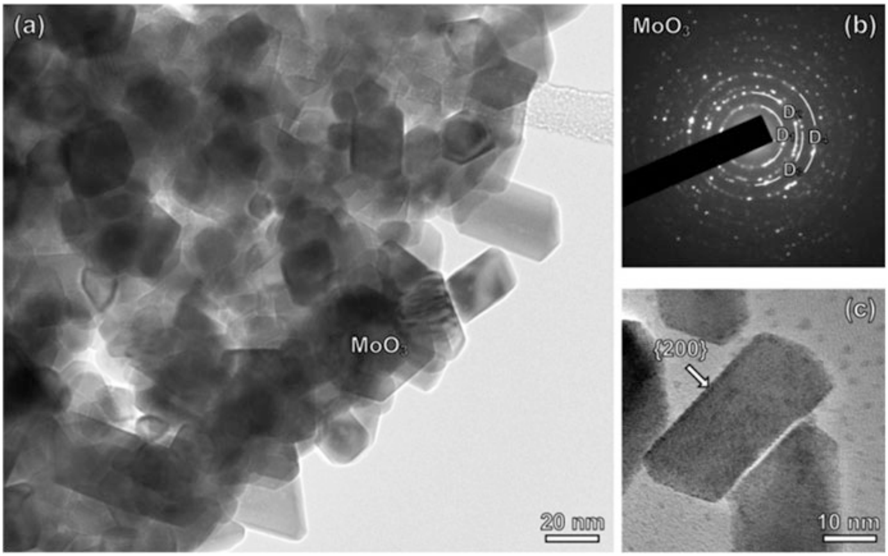

Fig. 8.33 (**a**) TEM image of euhedral MoO_3 nanocrystals in the sample with the Ni/Mo ratio 1/0.3. (**b**) Electron diffraction pattern from this area indicates the presence of monoclinic MoO_3 phase. The strongest SAED diffraction rings in the pattern correspond to $D_1 = \{200\}$, $D_2 = \{211\}$, $D_3 = \{220\}$, $D_4 = \{022\}$. (**c**) MoO_3 crystals are terminated with well-defined {200} dominating pinacoidal faces (Reprinted from Ref. [1] with kind permission from Springer)

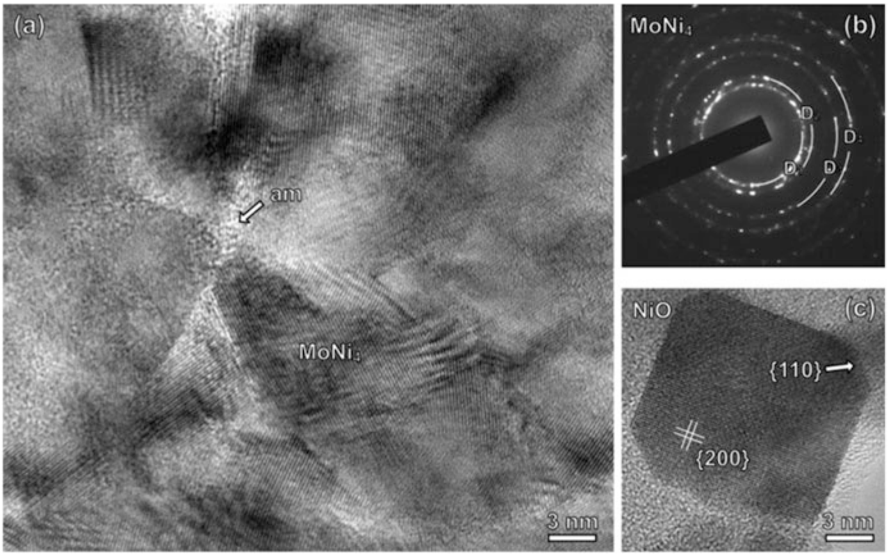

Fig. 8.34 (**a**) High-resolution TEM image of intergrown $MoNi_4$ nanocrystals. In the pockets of $MoNi_4$ grains, there are remnants of uncrystallized amorphous phase (am). (**b**) SAED pattern shows rings of high-intensity spots at reciprocal distances corresponding to $MoNi_4$ phase. The strongest reflections were indexed to $D_1 = \{211\}$, $D_2 = \{002\}$, $D_3 = \{132\}$, $D_4 = \{501\}$. (**c**) Idiomorphic NiO particle (rock-salt structure) with well-resolved {200} lattice planes. The crystal is faceted with cube {001} and dodecahedral {110} faces (Reprinted from Ref. [1] with kind permission from Springer)

to $D_1 = \{211\}$, $D_2 = \{002\}$, $D_3 = \{132\}$, $D_4 = \{501\}$ [21]. In some areas, we also find isolated crystals of NiO with a predominating cubic morphology and the edges truncated by rhombic dodecahedral faces. A close-up of a typical NiO nanocrystal is shown in Fig. 8.34c, showing well-resolved {200} lattice planes. The diffraction rings of the NiO phase cannot be seen most probably due to much stronger diffraction lines for the $MoNi_4$ and MoO_3 phases. Accordingly, its presence is determined by the measurement of *D* values, as shown in Fig. 8.34c [16].

On both SAED patterns, as well as on other SAED patterns, additional diffraction lines (more or less pronounced) are present, indicating that at the position of TEM analysis, other phases are also present (actually at each position of TEM analysis, a mixture of different phases exists), but the best defined are the ones determined by the analysis of the SAED patterns. Hence, it could be concluded that the $MoNi_4$ and MoO_3 phases prevail in the powder with high Ni content (electrodeposited at the Ni/Mo ratio 1/0.3), while some amount of NiO phase has also been detected.

The TEM Analysis of Electrodeposited Mo-Rich Mo-Ni-O Powders

A general appearance of Mo-rich sample does not differ much from the Ni-rich. The TEM of typical amorphous cluster is shown in Fig. 8.35a. In the small crystalline areas (x1), traces of $MoNi_4$ and MoO_3 phases were detected, and their diffraction

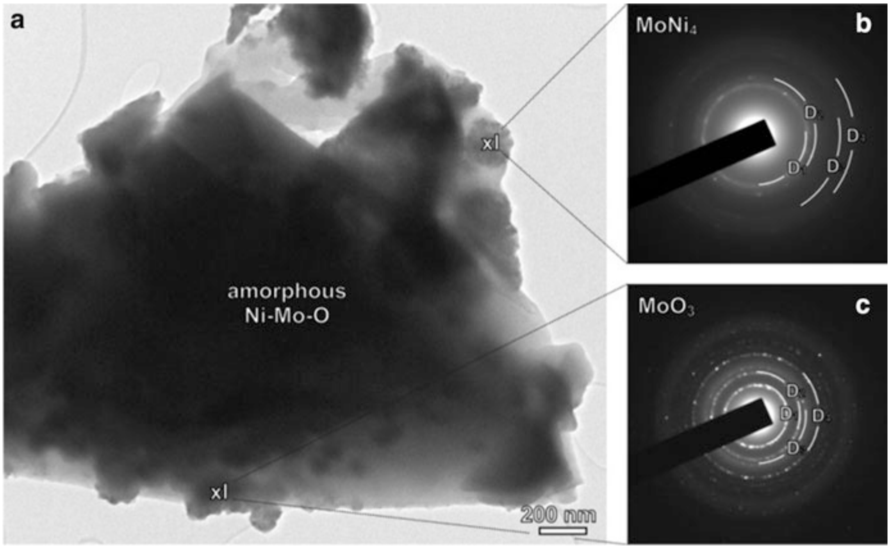

Fig. 8.35 (**a**) TEM image of the amorphous Mo-Ni-O cluster containing some crystalline areas in the powder electrodeposited at the Ni/Mo ratio 1/3. (**b**) SAED pattern from the area rich in $MoNi_4$ nanocrystals, similar to those in the Ni-rich sample, shown in Fig. 8.34. (**c**) SAED pattern of the area containing MoO_3 nanocrystals, similar to those in the Ni-rich sample, shown in Fig. 8.33 (Reprinted from Ref. [1] with kind permission from Springer)

patterns are presented in Fig. 8.35b, c, respectively. The diffraction lines in Fig. 8.35b are barely visible, indicating amorphous character of the $MoNi_4$ phase, while much stronger diffraction lines for the MoO_3 phase (Fig. 8.35c) indicate its more pronounced crystallinity. In this sample, the presence of NiO phase has not been detected.

It appears that in both samples, $MoNi_4$ phase is more strongly bound to the amorphous phase than the oxide phases. This might be the reason why in our previous investigation [1, 14, 15] this phase has clearly been detected by XRD in the recrystallized samples only after annealing at 600 °C, while at all other temperatures a broad peak around $2\theta = 44^\circ$ was only an indication of its existence.

It should be emphasized here that most of the phases detected in the recrystallized electrodeposited Mo-Ni-O powders [14, 15] ($MoNi_4$ and MoO_3) were also found in as-electrodeposited Mo-Ni-O powders, indicating their formation during the process of alloy electrodeposition.

Taking into account that NiO, MoO_3, and $MoNi_4$ phases were detected in electrodeposited samples by TEM, a new mechanism of Mo-Ni-O alloy electrodeposition (see Eqs. (7.20) and (7.23)) has been proposed.

References

1. Jović VD, Lačnjevac UČ, Jović BM (2012) Morphology, chemical, and phase composition of electrodeposited Co-Ni, Fe-Ni, and Mo-Ni-O powders. In: Djokić S (ed) Modern aspects of electrochemistry, vol 54. Springer Science + Business Media, New York, pp 251–343
2. Abd El-Halim AM, Khalil RM (1986) Some characteristics of Ni-Co alloy powders electrodeposited from dilute sulphate baths. Surf Coat Technol 27:103–115
3. Jović VD, Maksimović V, Pavlović MG, Popov KI (2006) Morphology, internal structure and growth mechanism of electrodeposited Ni and Co powders. J Solid State Electrochem 10:373–379
4. Jović VD, Jović BM, Pavlović MG, Maksimović V (2006) Morphology and composition of Ni-Co alloy powders electrodeposited from ammoniacal electrolyte. J Solid State Electrochem 10:959–966
5. Jović VD, Jović BM, Maksimović V, Pavlović MG (2007) Electrodeposition and morphology of Ni, Co and Ni-Co alloy powders part II. Ammonium chloride supporting electrolyte. Electrochim Acta 52:4254–4263
6. Jović VD, Jović BM, Pavlović MG (2006) Electrodeposition of Ni, Co and Ni-Co alloy powders. Electrochim Acta 51:5468–5477
7. Jović VD, Maksimović V, Pavlović MG, Jović BM (2006) Morphology and phase composition of Ni-Co alloy powders electrodeposited from ammonium sulfate-boric acid electrolyte. Mater Sci Forum 518:307–312
8. Lačnjevac U, Jović BM, Jović VD (2009) Morphology and composition of the Fe-Ni powders electrodeposited from citrate containing electrolytes. Electrochim Acta 55:535–543
9. Lačnjevac U, Jović BM, Maksimović VM, Jović VD (2010) An attempt to produce $NiFe_2O_4$ powder from electrodeposited Fe-Ni alloy powders by subsequent recrystallization in air. J Appl Electrochem 40:701–708
10. Zhelibo EP, Kravets NN, Gamarkin MY, Remez SV (1995) Theory, preparation technology, and properties of powders and fibers. Effect of heat treatment on the properties, structure, and

magnetic properties of Iron-Nickel alloys with micron particle size. Powd Metall Metal Ceram 34:113–116

11. Zhelibo EP, Kravets NN (1997) Theory, preparation technology, and properties of powders and fibers. Influence of the electrolysis temperature on the formation, composition, and magnetic properties of highly dispersed Iron and Iron-Nickel alloy powders. Powd Metall Metal Ceram 36:264–268
12. Chu CM (2003) The effect of complexing agents on the electrodeposition of Fe-Ni powders. J Chin Inst Engrs 34:689–695
13. Brenner A (1963) Electrodeposition of alloys, vol II, Priniciples and practice. Academic, New York
14. Jović BM, Jović VD, Maksimović VM, Pavlović MG (2008) Characterization of electrodeposited powders of the system Mo-Ni-O. Electrochim Acta 53:4796–4804
15. Lačnjevac U, Jović BM, Baščarević Z, Maksimović VM, Jović VD (2009) Morphology and phase composition of as-deposited and recrystallized Ni-Mo-O powders. Electrochim Acta 54:3115–3123
16. Jović VD, Jović BM, Lačnjevac U, Branković G, Bernik S, Rečnik A (2010) An attempt to predict the mechanism of Mo-Ni-O powders electrodeposition from the results of their TEM analysis. Electrochim Acta 55:4188–4193
17. Jović VD, Nikolić ND, Lačnjevac UČ, Jović BM, Popov KI (2012) Morphology of different electrodeposited pure metal powders. In: Djokić SS (ed) Modern aspects of electrochemistry, vol 54. Springer Science + Business Media, New York, pp 63–123
18. Kieling VC (1997) Parameters influencing the electrodeposition of Ni-Fe alloys. Surf Coat Technol 96:135–139
19. Zhou XM, Wei XW (2009) Single crystalline FeNi dendrites: large scale synthesis, formation mechanism, and magnetic properties. Cryst Growth Des 9:7–12
20. Popov KI, Djokić SS, Grgur BN (2002) Fundamental aspects of electrometallurgy. Kluwer, New York
21. Harker D (1944) The crystal structure of Ni_4Mo. J Chem Phys 12:315–320
22. Parise JB, McCarron EM III, Von Dreele R, Goldstone JA (1991) β-MoO_3 produced from a novel freeze drying route. J Solid State Chem 93:193–201